Modeling selective gating by nanopores with poly(ethylene glycol) and PEG-binding antibodies

Master's Thesis

Nanoscience Master of Science Curriculum

Biozentrum and the Swiss Nanoscience Institute

University of Basel

Janne Hyötylä

29.07.2009

Supervised by:

Prof. Dr. Roderick Lim

Abstract:
A major challenge in chemical engineering and biotechnology is the design of efficient and long-lasting selective membrane systems in applications such as water purification, medicinal systems, detection and filtration of hazardous substances. In biology, such functionality can be ascribed to the nuclear pore complex (NPC), which acts as the sole gatekeeper for all molecular traffic between the nucleus and the cytoplasm in eukaryotic cells. Natively unfolded protein domains anchored to the NPC, so-called FG-domains, are proposed to act as a polymer brush-like barrier to unspecific macromolecules while allowing the translocation of select cargo via interactions between soluble transport receptors and the FG-domains. Moreover, the NPC is not known to clog despite the complex cellular environment. In this work, we have constructed a synthetic system that seeks to mimic and test the key aspects of NPC functionality. Specifically, we have grafted poly(ethylene glycol) (PEG) to gold nanorings in order to replicate the overall topography and distribution of FG-domains at the NPC, and employed PEG-binding antibodies to mimic the receptor-FG interactions. The resulting biochemical interactions and nanomechanical effects are correlated using a setup consisting of an integrated atomic force microscope (AFM) and fluorescence microscope. In the absence of anti-PEG, we find that the terminally anchored PEG chains form a polymer brush that envelopes the entire nanoring. This provides a long-range steric repulsive barrier that minimizes the clogging of unspecific molecules at the pore. In comparison, we find that binding of anti-PEG to the PEG chains collapses the PEG brush and partially opens the pore. On a more technical note, the combination of nanofabrication, AFM and fluorescence allows for the simultaneous measurement of biochemical and nanomechanical interactions directly at the scale relevant to the questions at hand, without having to resort to macroscopic assays to measure nanoscopic mechanisms.

Contents

1 Introduction

Nanoporous filter membranes are widely used to purify or desalinate water into drinkable form (1, 2), to remove toxic and hazardous substances from the environment (3), or as part of protein purification and filtration procedures (4). For instance, water desalination remains a growing area economically and scientifically, with world-wide water consumption constantly increasing. Reverse osmosis (RO)-based membrane filtration has emerged as the leading technology, with 80% of water desalination plants using RO (5). The RO mechanism works by extracting salts and other solutes from water molecules by applying a pressure gradient across a membrane with extremely small pores. Water molecules are pushed across the membrane against their osmotic pressure, while ions, salts and larger molecules cannot permeate the membrane. Membranes for such filtering purposes are classified according to their approximate pore diameters: RO membranes $\lesssim 1\,\mathrm{nm}$, nanofiltration (NF) membranes $\sim 1 - 10\,\mathrm{nm}$, ultrafiltration (UF) $\sim 10 - 100\,\mathrm{nm}$, and microfiltration (MF) $\sim 10\,0 - 1\,000\,\mathrm{nm}$. MF and UF membranes are also used for protein separation and purification (for a review see (4)). MF membranes are commonplace in biological and medical laboratories to keep solutions free from particle aggregates. UF membranes are used to separate proteins of different sizes from solution such as in protein concentrators, dialysis systems, etc. where a certain size range of proteins are separated from the rest of the solution.

The working paradigm of the abovementioned membrane technology is mainly based on size exclusion across pressure gradients, possibly with electrostatic fields further hindering

or accelerating the flow of particles (i.e. charged membranes, or applied electric field across membranes). These membranes are physically constrained by a trade-off between selectivity and flux (the amount of material passing through the membrane in a given time). Larger pores allow higher flux but suffer from a reduction in molecular selectivity. A high variability in pore sizes also means that cut-off sizes are only approximately designed. One further major setback is membrane fouling. This occurs when organic, inorganic, and biological matter present in solution adsorb non-specifically on and in the membrane pores, thereby causing a reduction in flux and specificity. As a result, the membrane clogs (5–7). This problem is compounded as pore sizes decrease (i.e., in the nm regime) given the dominance of intermolecular and interfacial forces (e.g. van der Waals, electrostatic) at high surface area-to-volume ratios. Although there exist different countermeasures to reduce membrane fouling, such as placing NF or UF membranes in front of RO membranes to gradually filter out differently-sized particles, or adding chemicals (e.g. coagulation agents) to precipitate and remove contaminants, no method eliminates the problem completely except to replace the membrane (6, 8).

Remarkably, efficient, non-fouling, selective filtering is a hallmark of the eukaryotic cell. The nuclear environment of a cell is completely different from the cytoplasmic one, with DNA-related and transcriptional enzymes required in the nucleus, while the transcribed RNA is translated to proteins in the cytoplasm. Hence, the compartmentalization of the cell into the nucleus and cytoplasm by the nuclear envelope is essential for cellular function. In this regard, the cell has evolved mechanisms to keep this order intact while allowing for the efficient transport of macromolecules to their specific target compartments.

Molecular transport across the nuclear envelope occurs exclusively through $\sim 50\,\mathrm{nm}$ wide perforations in the nuclear envelope known as nuclear pore complexes (NPC) (9, 10). Although small molecules (e.g. ions) can diffuse passively through the pore, the passage of non-specific macromolecules is thought to be impeded by the presence of a polymer

brush-like barrier that is made up of several natively unfolded proteinaceous domains (FG-domains) (11, 12). The passage of macromolecules is restricted to cargo-carrying transport receptors that exhibit biomolecular interactions with the NPC. Paradoxically, such a mechanism is not governed by size exclusion (i.e., transport receptors effectively double the cargo mass) but by biochemical interactions (see section 2.1 for details). Moreover, an understated characteristic of the NPC lies in its apparent lack of clogging in vivo despite being surrounded by a complex biomolecular environment.

Here, the driving impetus behind this master's thesis is to construct and evaluate a synthetic nanopore that exploits the basic NPC mechanism to control transport. As shown in Fig. 1.1, our NPC-inspired nanopore is constructed using completely synthetic materials. Using nanofabrication, we have constructed gold nanorings on glass slides that mimic the NPC dimensions. Based on its excellent (i.e. non-fouling) protein-repelling and surface-passivating properties (13, 14), we have grafted poly(ethylene glycol) (PEG) chains to the nanorings to replicate the role of the FG-domains in the NPC selective gating mechanism. To fulfill the role of a transport receptor, we have used fluorescently labeled antibodies that are specific against PEG. Hence, we hypothesize that (i) the PEG forms a polymer brush barrier at the nanopore; (ii) only antibodies can access the nanopore by causing the PEG barrier to collapse; (iii) non-specific macromolecules will not clog the nanopore. Table 1.1 summarizes the similarities and differences between the NPC and our PEG nanopore.

By combining atomic force microscopy (AFM) and fluorescence microscopy we have correlated the nanomechanical properties of the PEG chains to biochemical interactions with the anti-PEG. In the absence of anti-PEG, we show that the PEG forms a brush-barrier over the nanoring. This brush-barrier collapses in the presence of anti-PEG. Moreover, we have obtained important evidence from control studies using secondary antibodies that show lack of binding to PEG in the absence of primary anti-PEG. While this is to be determined, this suggests that the primary and secondary antibodies can

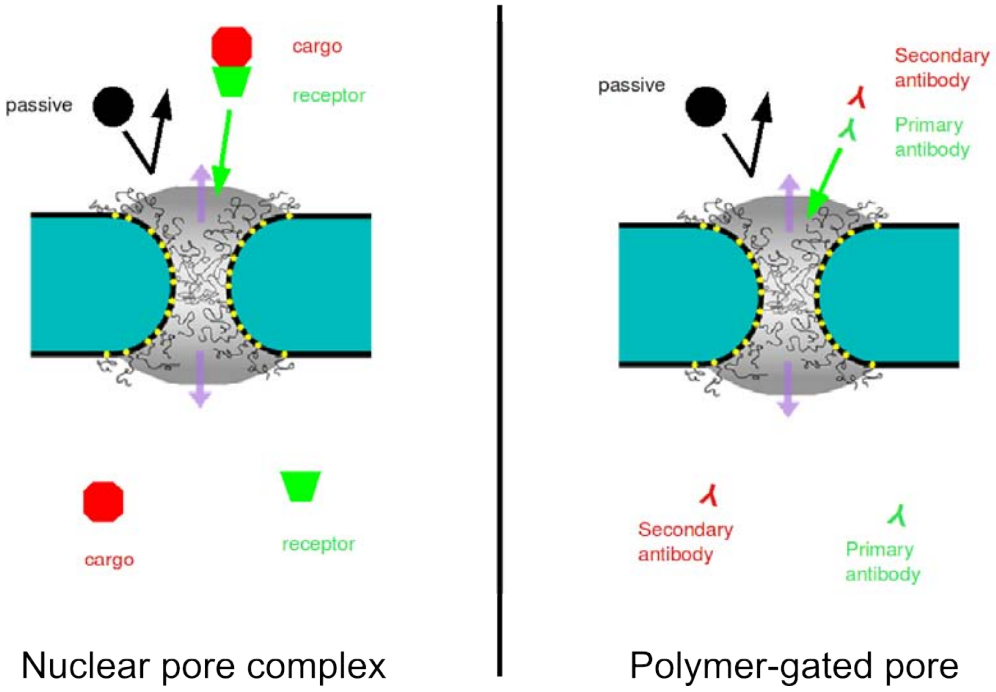

Figure 1.1: Comparison between the nuclear pore complex and a NPC-inspired synthetic nanopore. Note that both drawings are similar, except that we have (i) replaced the FG-domains with PEG, (ii) the transport receptor with anti-PEG, and (iii) the cargo with a secondary antibody. A priori, the PEG brush should repel non-specific "passive" molecules from the vicinity of the pore. Selective translocation through the pore is limited to the anti-PEG due to specific interactions with the PEG backbone.

Table 1.1: Comparison of the applications and limitations of current polymer-based nanopores versus the NPC and novel PEG-based nanopores inspired by the NPC.

	NPC	**current synthetic nanopores**	**new NPC-inspired PEG nanopores**
size	50 nm	1 – 1000 nm	10 – 100 nm
pore material	unfolded polypeptides	polymers (e.g. PMMA, PVC, PVA)	PEG
used for	selective transport	flow control, size separation	selective transport
fouling / clogging	none reported	yes	no (?)
solvent change	open ↔ close	open ↔ close, no effect, or clogging	open ↔ close
transport receptors	yes	no	yes
references	(9–12, 15)	(4–6)	–

assume the role of transport receptor and cargo, respectively.

These results indicate that a synthetic nanopore based on the NPC is feasible and demonstrates how cellular nanomachines can offer novel technological strategies provided that their mechanism can be first understood and replicated. On a more technical note, our combination of nanofabrication, AFM (i.e. mechanical and force measurements) and fluorescence (i.e. localizing, visualizing biochemical interactions) is ideal to study nanoscale phenomena which might be difficult to access and characterize with "standard" macroscopic assays.

2 Background

2.1 The nuclear pore complex and nucleocytoplasmic transport

The nuclear pore complex (NPC) is a large multi-protein complex with a total mass of $\sim 120\,\mathrm{MDa}$ in vertebrates and $\sim 60\,\mathrm{MDa}$ in yeast that perforates the nuclear envelope separating the cytoplasm from the nucleus. The NPC's central pore is $\sim 50\,\mathrm{nm}$ deep and has an approximate hourglass cross-section which is $\sim 40\,\mathrm{nm}$ wide at its narrowest part (9, 16, 17). The NPC consists of about 30 different proteins in multiple copies, called nucleoporins (nups) and displays an eight-fold rotational symmetry around the pore (10). Interestingly, only small molecules $< 40\,\mathrm{kDa}$ are allowed to freely diffuse through the NPC. The key NPC components responsible for the regulation of nucleocytoplasmic transport of macromolecules are several proteinaceous domains rich in phenylalanine-glycine (FG-)repeat motifs (FG-domains) which are found on $\sim 30\,\%$ of all nups (9, 18, 19). The FG-domains lack secondary structure, i.e. they are "natively unfolded" (15) or "intrinsically unstructured" (20), and physically resemble a random coil or worm-like-chain (21). This is because the FG-domains are comprised of mainly neutral or hydrophilic peptides between the (hydrophobic) FG-repeat motifs. Importantly, the FG-domains are anchored in and around the NPC on one end through folded domains that integrate within the NPC. In this manner, the FG-domains have been suggested to impose a physical barrier against unspecific macromolecules in the form of a polymer

brush (11, 12). Owing to the long-range repulsive properties of the brush, unspecific molecules are repelled from the entrance of the pore, preventing the pore from clogging.

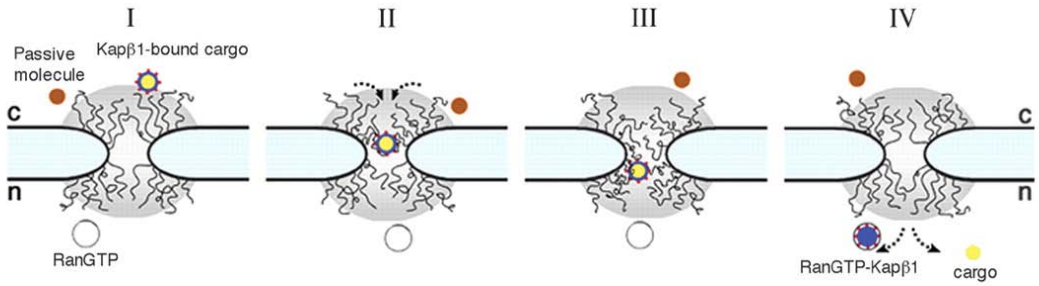

Figure 2.1: Working hypothesis of the nucleocytoplasmic transport as the basis for this work. **(I)** Passive cargo is rejected from the vicinity of the pore by the entropic steric repulsive brush. **(II, III)** Importin β (here called kapβ1) with a bound cargo translocates through the pore by inducing collapse in the FG-domains it interacts with. Importin β has several binding sites for FG-repeats and is able to interact with multiple FG-domains at the same time, which is hypothesized to be a key factor in aiding the collapse. **(IV)** Once passed through the pore, importin β is sequestered away by RanGTP and the cargo can diffuse to its target in the nucleus. Figure taken from (12).

In the case of nuclear import, only macromolecules bearing a nuclear localization signal (NLS) are recognized by and form complexes with transport receptors, e.g. importin β, can penetrate the FG-domain barrier and translocate through the NPC (Fig. 2.1). This occurs because the importins exhibit binding interactions with the FG-repeats which results in a collapse of the FG-domains to their anchoring sites (i.e. the pore is now "open") (12). It is noteworthy that one importin β protein has $\sim$10 hydrophobic binding pockets that can bind to individual FG-repeats (22–25). This means that transport receptors can bind to several FG-repeats, and an FG-domain can bind to several transport receptors at the same time. This promiscuity could lead to a loss of conformational entropy for the polypeptide chain so that a collapse is energetically more favorable. Once the importin-cargo complex has translocated through the pore, RanGTP binds to importin β and causes a dissociation of the cargo. The cargo is now free to diffuse to its target in the nucleus. It should be noted that although there are other NPC models in

the literature (18, 26), the basis of our current work is to evaluate the reversible collapse of a polymer brush and its effect on selective transport.

2.2 Polymers and polymer brushes

Polymer brushes form when polymers are anchored on one end to a surface or interface at a high enough density (27). In solution or at low grafting densities, polymers tend to assume random-walk configurations to maximize their configurational entropy as well as maximize the energetically favorable interaction with a good solvent. The typical polymer dimension is then its radius of gyration

$$R_g = aN^{3/5}\,, \tag{2.1}$$

with a being the persistence length and N the number of subunits. When a polymer is anchored on one end to a surface, it forms a so-called mushroom with dimension R_g. If the distance between surface-attached chains becomes smaller than $2R_g$, the polymer chains cannot satisfy both conditions – maximal configurational entropy and interaction with solvent – at the same time anymore. As a trade off the chains start to stretch perpendicularly away from the surface and form a polymer brush (28–30). The simplest model of polymer brushes which has proven to be experimentally valid was developed by de Gennes and Alexander (31, 32) and regards the brush as an entropic spring stretched to the height h. The decrease in entropy and increase in unfavorable chain-chain interactions leads to a free energy cost per chain, which when minimized leads to a predicted brush height, for good solvents (30):

$$h \approx N\,(a/d)^{2/3} \tag{2.2}$$

with d being the average grafting distance at the surface. Remarkably, the brush height scales linearly with N, while the radius of gyration only scales with $N^{3/5}$. This means

that a polymer brush can extend very far from the surface, given a high enough grafting density.

Poly(ethylene glycol) or PEG (also referred sometimes to as PEO or poly(ethylene oxide)) is a hydrophilic polymer consisting of ethylene glycol units ($-CH_2-CH_2-O-$). Importantly, it is fully biocompatible, meaning that it does not elicit an immune response in biological hosts (33) and does not adsorb proteins in solution or as a brush when end-grafted to a surface (13, 14). These properties are believed to stem from the excellent hydration properties of PEG (34). The backbone of PEG has similar structural properties as water, allowing water and PEG to interact via strong hydrogen bonding. The strong interaction with water adds additional energy costs to displacing some of the available volume for PEG e.g. by proteins, leading to a repulsive force against the proteins and thus to its protein rejection and anti-fouling properties.

In our experiments we use 20 kDa mPEG-SH which are chemically modified PEG chains to have an inert methyl group on one end and a thiol group on the other end (Fig. 2.2). The size of a PEG monomer is 2.8 Å (35), the PEG chain persistence length is 3.5 to 3.8 Å (35, 36), and 20 kDa mPEG-SH chains have on average $\sim$450 subunits. The persistence length of FG-domains and other unfolded polypeptide chains is $\sim$4 Å (21, 37, 38), and some FG-domains have a similar number of subunits (i.e. amino acids) as 20 kDa mPEG-SH (39). This makes our use of PEG structurally comparable to FG-domains in the NPC, in addition to its protein-repelling capacity.

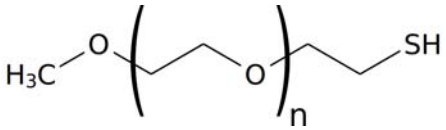

Figure 2.2: Chemical formula of mPEG-SH. 20 kDa chains with $n \approx 450$ were used in this work.

2.3 Applications of PEG and PEG brushes

Owing to its anti-fouling and protein-repellent properties, PEG is widely used for surface passivation. Filtration membranes coated with PEG show to exhibit a reduction in fouling (40, 41). PEG-coated surfaces show resistance against cells and bacteria and are used to prevent bacterial film growth e.g. on biological implants (42–44).

Today PEGylation research, i.e. the attachment of PEG chains to other molecules, is a very active field and has resulted in first clinical trials for drugs (45). Foreign PEGylated proteins do not show to stimulate an immune response against them, in contrast to unmodified proteins (46). Due to ease of preparation, PEG chains can be attached to a variety of different targets: small drug molecules (45), nanoparticles (47, 48) and liposomes (49) that encapsulate or display the therapeutic substance, proteins such as antibodies (50, 51) and even oligonucleotides (52) – for an overview see (53). The PEGylated conjugates are also called "stealth" particles because they can avoid or escape the host's immune response. PEGylated particles also survive longer in the blood stream because of their bigger size, thus avoiding to get filtered out by the kidneys. In some cases, the half-life of a drug in the blood can increase from a few minutes to over 24 hours by PEGylating the drug (45).

2.4 Antibodies, Anti-PEG

Antibodies are proteins and form one of the main constituents of the vertebrate immune system. Antibodies have an extremely variable binding pocket, so that they can be designed or tailored to bind almost any structure, then called antigen (54). Antibodies belong to the Immunoglobulin (Ig) family of proteins that are circulating in the body. The main members of this family are IgG, IgM and IgA. The structure of IgG (Immunoglobulin G) is shown in Fig. 2.3. As can be seen, each IgG has two variable fragments (F_v) where the binding pocket to the antigen is located. The local structure

or sequence that the antibody recognizes is called epitope.

The constant F_c region of the IgG gets recognized by receptors on different cells once an antibody has bound its antigen, thus triggering further immune responses. In this way, the immune system reacts to molecules, proteins, particles, etc. which it has recognized as foreign and potentially hazardous to the body by activating different cells and signal cascades to neutralize or remove the foreign objects. By binding to foreign substrates, antibodies promote the aggregation and deactivation of active molecules. Furthermore, they mark the particles as foreign for other components of the immune system. IgG is by far the most common antibody type used in research, and it is also used in this work. The other immunoglobulins differ in their overall structure, e.g. IgM has five binding sites instead of two.

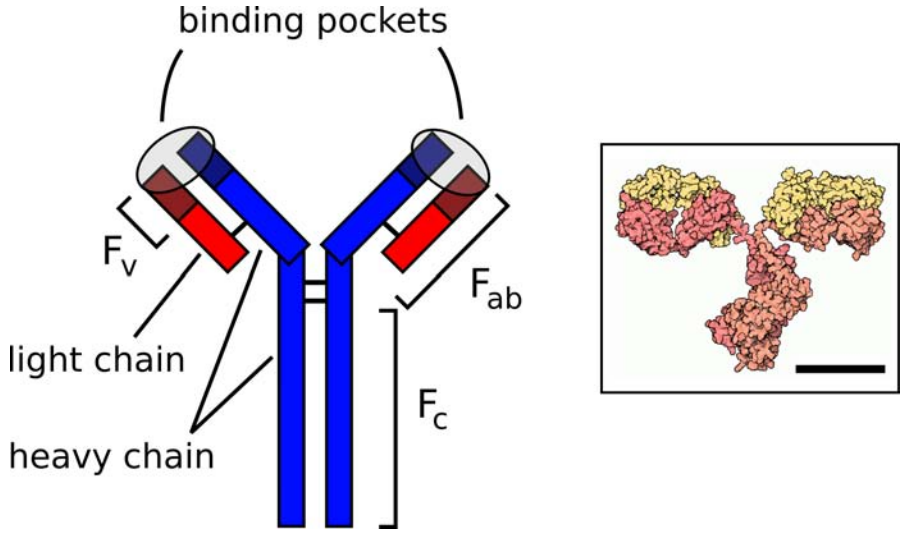

Figure 2.3: Left: IgG antibody structure. The antibody consists of 4 peptide chains: two heavy chains (blue) and two light chains (red). One heavy and light chain are each linked together via disulfide bonds. The F_c and F_{ab} fractions are linked together via flexible hinges. The antigen recognition site is located in the variable fraction F_v between the heavy and light chains near the N terminus. The molecular weight is $\sim 150\,\mathrm{kDa}$ and the antibody spans $\sim 10\,\mathrm{nm}$ along its vertical axis. Right inset: Realistic volume rendering of an IgG molecule, based on an x-ray crystal structure (adapted from (55)). Scale bar, 5 nm.

Secondary antibodies are antibodies that themselves recognize the F_c part of other

antibodies. They are a valuable tool in biochemistry since they can be conjugated to a read-out marker (e.g. fluorescent molecule) and used to detect the presence of primary antibodies (i.e. those that recognize the specified epitope). In this way, one batch of marked secondary antibodies can be used to detect many different primary antibodies without needing perform potentially difficult labeling reactions on the valuable primary antibodies themselves. Moreover, as multiple secondary antibodies can bind to a primary one, they enhance the read-out signal.

While monoclonal antibodies (mAbs) (56) are a standard tool for biochemical assays (immunohistochemistry, immunofluorescence), they are being used increasingly for disease therapy in humans, from cancer to rheumatoid arthritis (a small sample of reviews: (57–59)). Since PEGylation of drugs and drug delivery systems is being increasingly used as well, there have been efforts to produce mAbs that act against PEG (60–64). Anti-PEG mAbs are used to measure the levels of a PEGylated drug circulating in a host. By simply adding biocompatible PEG chains to any drug, it becomes easy to monitor the half-life and secretion of the drug by probing the blood serum with anti-PEG. It has also been shown that anti-PEG accelerates the clearing of a PEGylated drug from the blood (60, 62). PEGylation was shown to increase the uptake of drugs in a tumor compared to normal tissue. Subsequent administration of anti-PEG efficiently cleared the drug from normal tissue but not from the tumor, thus decreasing negative side effects of anti-tumor drugs.

In this work, we use the monoclonal IgG anti-PEG "E11" (60) to simulate a transport receptor binding to FG-domains. Similarly to the NPC where the FG-repeats are distributed along the whole FG-domain, E11 anti-PEG binds the backbone of the PEG-chain and thus has enough binding sites available over the length of the whole chain. In contrast to the NPC where binding affinities are rather low, the antibody is designed to bind very strongly to PEG to be able to detect even very small quantities of PEG e.g. in drug delivery applications.

3 Materials and Methods

3.1 Fabrication of Au nanorings

Arrays of 20×20 gold nanorings were fabricated by electron beam lithography (EBL) and subsequent evaporation on 0.2 ± 0.02 µm thick standard microscopy cover glass slides (round, 24 mm diameter; Karl Hecht Assistent, Germany). During EBL (Fig. 3.1), a focused electron beam impinges a polymer resist on top of the sample at areas where the final structure should later appear, a process called exposure, in analogy to the exposure of a film by photons in conventional lithography. The energy of the incoming electrons breaks the polymer bonds of the resist. During development, the exposed parts of the resist are removed from the sample, while the stronger interlinked non-exposed areas of the polymer remain on the chip. At the next step, gold is evaporated onto the whole area. The lift-off process removes the remaining resist together with anything evaporated on top of it, thus leaving only the designed sample structure on the chip, i.e. the nanorings.

Before applying the polymer resist, each chip was thoroughly cleaned by ultrasonicating in acetone and isopropanol (IPA), followed by thorough rinsing with deionized (DI) water and drying with N_2. 950 kDa poly(methyl methacrylate) (PMMA) was spin-coated at 5000 rpm onto the substrate to create a 350 nm thick polymer resist layer for EBL. After spinning, the sample was placed into an oven and baked for 15 min at 170 °C, driving off excess solvent to improve the final structure quality. After preparing the resist layer, EBL was performed with an Elionix ELS-7000 (Elionix, Japan) EBL system. The nanoring structures with nominal inner and outer diameters of 80 nm and 400 nm and 1.3 µm

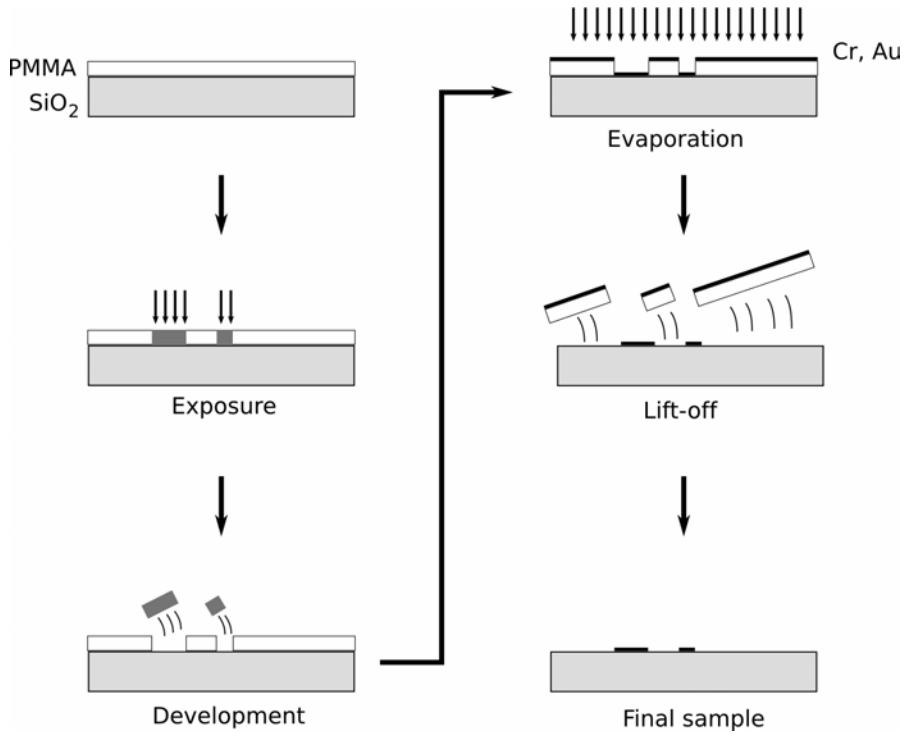

Figure 3.1: Principle of the nanofabrication process by electron beam lithography (EBL) and thermal evaporation. The PMMA resist on top of the glass slide gets exposed by an electron beam. The exposed area is removed during the development. An adhesion layer of Cr, followed by the desired thickness of Au, is evaporated over the whole sample. Afterwards, the lift-off removes the rest of the resist, leaving only the final structure on the sample.

pitch between rings were exposed at a dose of 800 µC/cm^2 by using an electron beam with acceleration voltage of 100 kV and a beam current of 20 pA. After exposure, the sample was developed in a solution of 3 parts IPA and 1 part methyl isobutyl ketone (MIBK) for 70 s, followed by rinsing in IPA and DI water for 20 s each and drying with N_2. An adhesion layer of ∼5 nm Cr and the main structure of ∼30 nm Au was deposited on the samples by thermal evaporation. The lift-off was performed by soaking in acetone for 10 min and final rinsing in acetone, IPA and DI water, followed by drying the sample with N_2.

3.2 Sample functionalization and preparation

Glass slides were sequentially cleaned in glass beakers by ultrasonication for 20 minutes in acetone, IPA, and ethanol to remove dust particles and other contaminants before functionalization. All glassware was cleaned beforehand by ultrasonication and boiling in IPA and ethanol. Samples were dried with N_2 after each sonication step. The samples were then further cleaned in UV-ozone (UVO Cleaner 42-220, Jelight, USA). In the UVO cleaner, a constant flow of O_2 into the sample chamber gets ionized by the simultaneous UV radiation, creating ozone and oxygen radicals which react with any organic molecules on the sample surface. The reactants (e.g. CO_2, H_2O, etc.) desorb from the sample into the gas phase. The UVO cleaning was followed by another ultrasonication step for 30 minutes in ethanol.

After drying with N_2, the nanostructures were immediately immersed under 60 µl of 1 mM 20 kDa thiolated methoxy-poly(ethylene glycol) (mPEG-SH, Laysan Bio, USA). 1 mM Tris(2-carboxyethyl)phosphine hydrochloride (TCEP, Sigma-Aldrich, USA) was added to the solution to prevent oxidation of the PEG thiols and the formation of disulfide bonds. The sample was left immersed for at least 12 hours at room temperature to ensure maximal surface coverage of the nanorings by covalent binding of the mPEG-SH to gold. Afterwards, the sample was rinsed with DI water (resistivity 18.2 MΩ cm, Milli-

Q purification system, Millipore, USA), and ultrasonicated in DI water for 10 seconds to remove non-covalently bound PEG chains. The sample was immediately used for measurements.

The hydrodynamic radius of PEG in solution was measured by dynamic light scattering (Zetasizer Nano, Malvern, UK). 20 kDa mPEG-SH ($\sim$450 subunits) in PBS with TCEP yielded a radius of 3.4 ± 0.3 nm with a polydispersity index (PDI) of 0.11 ± 0.03, where PDI < 0.1 signifies a very homogeneous sample. Both the radius and the PDI were extracted from autocorrelation curves of the scattered light signal by the cumulants method (for details see e.g. (65)).

3.3 PEG antibodies

To achieve biochemical binding specificity, PEG-binding monoclonal mouse IgG1 antibodies ("Anti-PEG E11") provided by S. Roffler were used (60). The antibodies were fluorescently labeled with Alexa Fluor 488 TFP ester (Invitrogen, USA). Prior to labeling, the antibody concentration was measured by an UV/VIS spectrophotometer (HP 8453, HP/Agilent Technologies, USA), using the absorbance at 280 nm wavelength and the IgG extinction coefficient of $203\,000\,\mathrm{M}^{-1}\,\mathrm{cm}^{-1}$. Typically 100 µl at 1 mg/ml were labeled in one batch. The labeling reaction was performed at 4 °C over night in PBS solution at pH 7.2 with 10:1 dye:antibody molar ratio, allowing attachment of the dye ester to the N termini of the IgG via a stable peptide bond. The reaction was stopped by adding 1.5 M hydroxylamine at pH 8.5 with 200:1 molar ratio of hydroxylamine:dye for one hour at room temperature. The labeled protein was then purified from free dye and stopping reagent using a size exclusion spin column designed specifically for IgG purification (Pro•Spin Kit CS-800, Princeton Separations, USA). UV/VIS spectrophotometer absorbance measurements confirmed successful labeling and the degree of labeling was determined to be 3 – 4 fluorophores per antibody by comparing absorption at 280 nm (protein) and 494 nm (dye).

The anti-PEG specificity of labeled antibodies was confirmed by a standard dot blot (Fig. 3.2). mPEG-SH at different concentrations (1 µl per dot) was applied on dry nitrocellulose membranes, 0.45 µm pore size, then left to dry overnight. The membranes were rehydrated in PBS with 0.1 % (v/v) Tween-20 at room temperature, blocked with 5 % (w/v) non-fat milk in PBS, then incubated with anti-PEG or unspecific control antibodies at 4 ℃ overnight. After primary antibody incubation, the membranes were washed in PBS/Tween and milk and incubated with the secondary antibody, rabbit anti-mouse-IgG alkaline phosphatase, for 1 h at room temp. After washing in PBS/Tween and assay buffer, CDP-Star chemiluminescent substrate (Applied Biosystems, USA) was added onto the membranes for 5 min. X-Ray-sensitive films were exposed with the membranes and developed, leaving a dark image on the film where the alkaline phosphatase activated the CDP-Star reagent, signifying presence of primary and secondary antibodies.

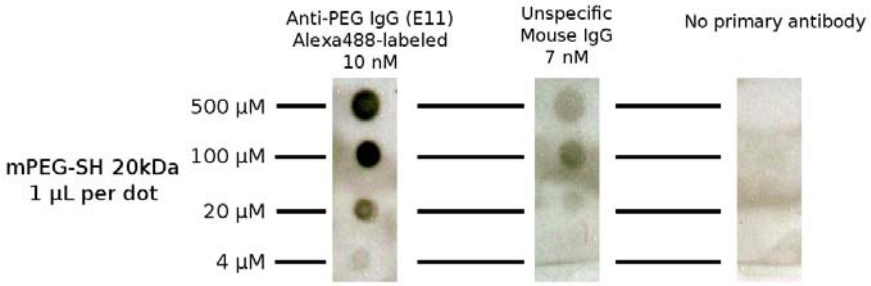

Figure 3.2: Dot blot binding assay of fluorescently labeled Anti-PEG E11 IgG antibodies. The dot blot confirms that the anti-PEG retains its binding affinity to PEG when conjugated to fluorescent dyes.

Labeled anti-PEG E11 was stored at 4 ℃ and measurements were carried out within a week from the labeling.

3.4 Atomic force microscopy

Atomic force microscopy (AFM) applies a nanometer-sized probe at the end of a flexible beam, or cantilever, which is free at the probe end and fixed at the opposite end.

The probe, usually in form of a sharp pyramidal tip, is scanned over a sample surface, maintaining contact with the sample. Any forces acting on the cantilever during scanning translates to a bending of the cantilever. The bending is detected by a laser beam focused on the top side of the cantilever which is reflected onto a position-sensitive detector (see Fig. 3.3). Because of the long laser beam path, very small sub-nanometer movements of the cantilever are detectable by the detector. By segmenting the detector into 4 parts, vertical and torsional movements of the cantilever can be separated by subtracting corresponding segment signal intensities (vertical: top half − bottom half signal; torsional: left − right signal). One of the basic applications of the AFM is imaging the height of surface features by scanning the tip over the surface and measuring the vertical beam deflection (contact mode). While the high vertical (z) resolution is attributed to the laser detection system, almost equally high lateral (x, y) resolution is achieved by the small probe size. When using sharpened pyramidal tips, the tip radius lies in the range of 5 – 30 nm, allowing for accurate imaging of features of similar dimensions.

The x, y, and z position of the cantilever is controlled by piezoelectric crystals ("piezos"). Piezos change their extension in one direction when an electric field is applied across the crystal in that direction. The extension of the piezos can be controlled to sub-nm accuracy which makes it possible to scan the tip accurately over very small areas.

The cantilever can be regarded as a spring obeying Hooke's Law, i.e.

$$F = kd\,, \tag{3.1}$$

where the acting force F on the cantilever is the result of the bending distance d and the cantilever's spring constant k. By calibrating the vertical deflection sensitivity

$$s = d/V\,, \tag{3.2}$$

i.e. the conversion of the raw voltage signal from the laser detector, V, to the cantilever

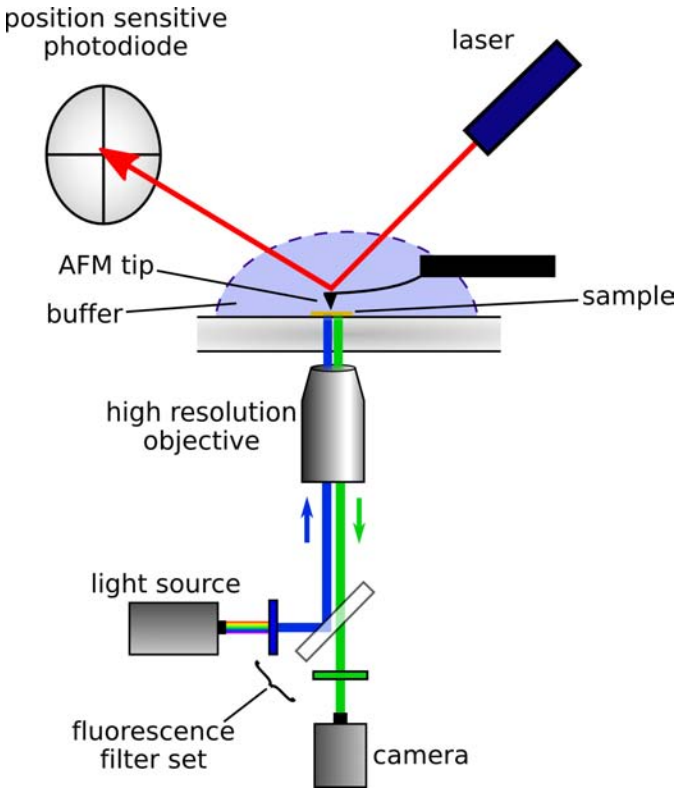

Figure 3.3: Combining atomic force microscopy (AFM) and fluorescence microscopy. The AFM, depicted schematically by the cantilever and the laser, sits on top of the inverted microscope sample stage. This allows for AFM and fluorescence measurements to be made under identical measurement conditions at a specific sample position.

bending distance d, we are able to directly measure the forces acting on the cantilever, making the AFM a unique tool not only for high-resolution imaging of surface features but also for measuring local forces between the tip and the surface. See Fig. 3.4 for an example of a local force measurement in one spot of a hard sample. The slope of the approach/retract curve when the tip is in contact is directly used as the calibration for the deflection sensitivity, since the cantilever bending d is the same as the z piezo movement towards the sample because the tip is in contact with the hard sample and does not move. A force curve measurement can be transformed into a force-distance curve where the force acting on the cantilever is plotted against the real distance of the tip from the sample surface (Fig. 3.5). This is accomplished by subtracting the cantilever deflection at each point from the piezo height. This way a hard surface is represented by a vertical force curve (i.e. infinite slope) and softer surfaces have smaller slopes. The slope of a force-distance curve can be directly used to calculate the stiffness of the sample at the probed point.

AFM measurements were performed using a Bioscope 2 with the Nanoscope V controller (Veeco, USA) sitting on top of an inverted optical microscope (Fig. 3.3). All measurements were done in contact mode, XY closed loop turned on, with a standard liquid cantilever holder in phosphate-buffered saline solution (PBS, 1.5 mM KH_2PO_4, 2.7 mM Na_2HPO_4, 155.2 mM NaCl, pH 7.2; Invitrogen, USA). Typical scan rates were 0.8 – 1.5 Hz. Rectangular Si_3N_4 cantilevers with a sharpened pyramidal tip (Biolever BL-RC150VB, Olympus, Japan) were used for imaging. Typical dimensions according to the manufacturer are: cantilever width 30 µm, length 100 µm, thickness 0.18 µm, and tip height 7 µm. The tip radius was determined representatively for two tips by scanning electron microscopy to be $\sim$25 nm. Fig. 3.6B shows a bright field image of the Biolever on top a nanoring array. Fig. 3.7 shows scanning electron micrographs of the Biolever tip.

Prior to the use of each cantilever, the spring constant was measured using the ther-

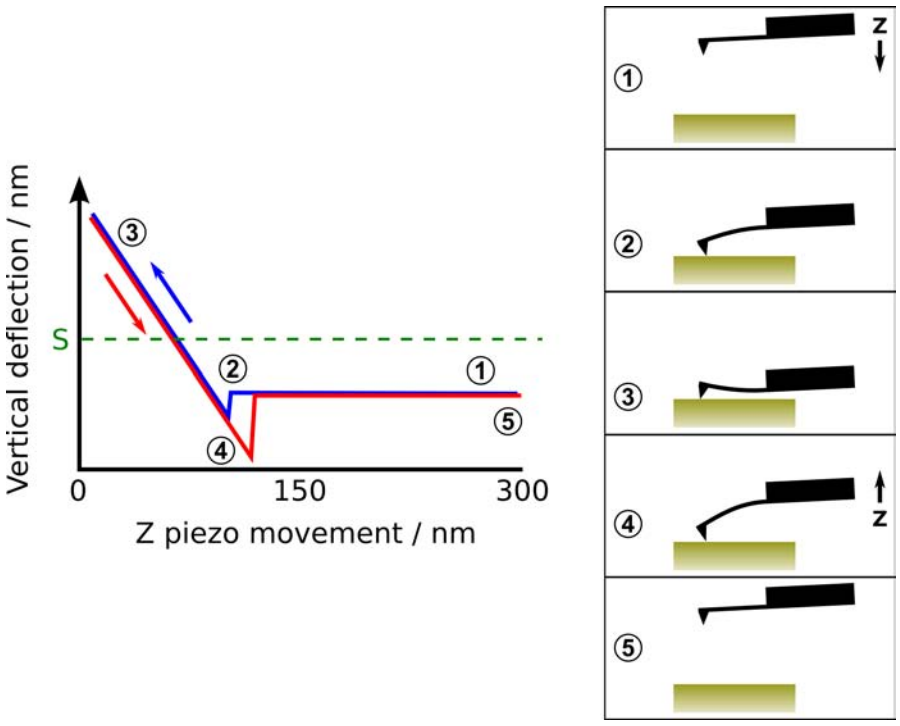

Figure 3.4: An example of a force vs. piezo-displacement curve recorded on a hard surface in H_2O. The cartoons on the right show the state and position of the cantilever corresponding to the numbers on the curve. **(1)** The z piezo ramps downwards and the approach force curve recording starts (blue curve). As long as the tip feels no force from the surface there is no change in deflection of the cantilever. **(2)** The tip is near the surface and slightly snaps downwards as an effect of electrostatic and van der Waals forces acting between surface and tip. **(3)** The cantilever deflects linearly in the positive direction as the z piezo moves downwards because the tip is in contact with the sample. At a predetermined point the z piezo direction is reversed (i.e. retraction; red curve) **(4)** The tip feels an increased adhesion (i.e. attraction) to the surface due to the increase in contact area upon surface compression. **(5)** Once the bending force of the cantilever becomes greater than the surface attraction of the tip,the tip snaps off the surface and returns to the zero-force baseline as it retracts from the surface. S denotes an adjustable setpoint for imaging in constant force mode. When imaging in this mode, the tip scans over an area keeping the deflection or force at the set value, adjusting the z piezo height as necessary. Constant force mode allows setting exactly the desired force during scanning over the surface and is used throughout this work.

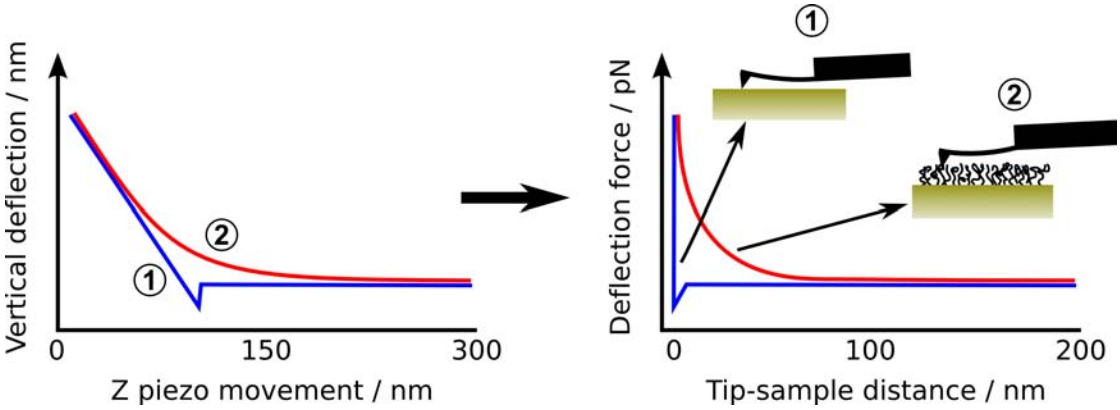

Figure 3.5: Two recorded approach force vs. piezo-displacement curves are transformed into force vs. tip-sample distance curves. The cantilever deflection is subtracted from the piezo position, yielding the direct tip-sample distance. The vertical deflection multiplied by the cantilever spring constant gives the force acting on the cantilever. On a hard substrate (1), no force is acting on the cantilever until contact with the surface (which is defined as tip-sample distance = 0). With soft material on top of the substrate (2), a repulsive force is measured at tip-sample distances greater than zero. The curve becomes vertical when the force on the tip is large enough to penetrate the soft material, resulting in contact with the underlying hard surface.

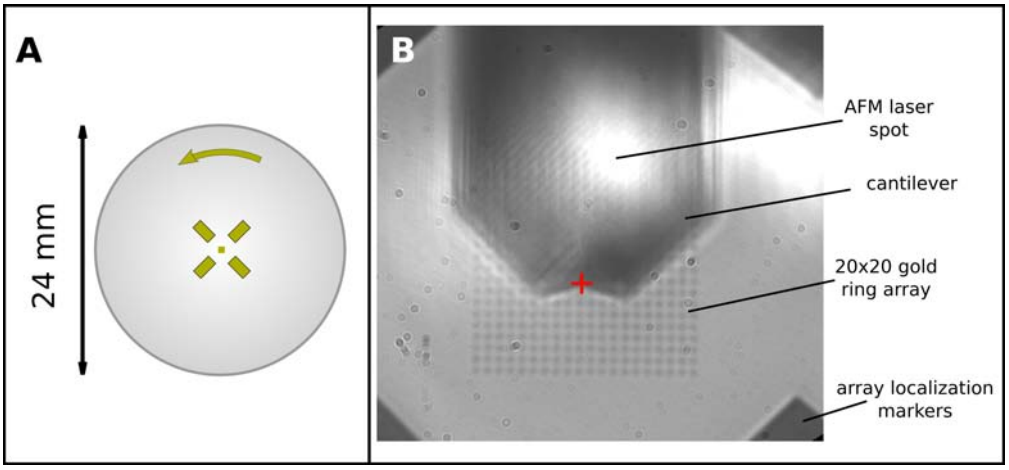

Figure 3.6: **A.** Layout of the glass slide with nanofabricated gold rings at the center. Around the nanoring array are 4 bigger gold markers to facilitate localization of the array under the microscope. The arrow at the top denotes the correct side of the glass slide. Gold structures are drawn in exaggerated size. **B.** Bright field image of the cantilever over the nanoring array. The red cross marks the tip apex position. Image taken with a 63× dry objective.

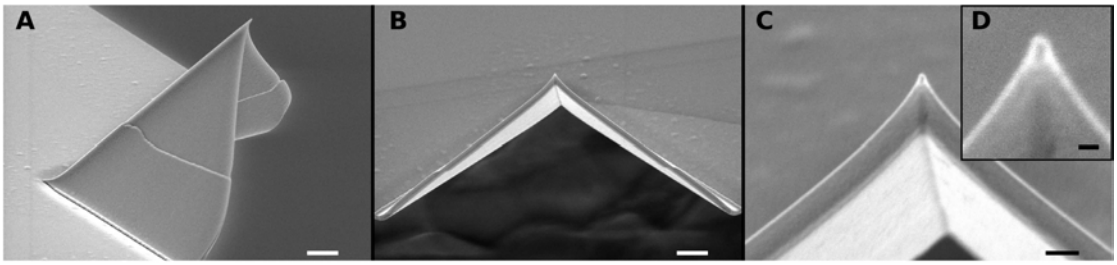

Figure 3.7: Scanning electron micrographs of the "arrowhead" type cantilever used for measurements (Olympus Biolever). **A.** Side view, scale bar 1 µm. **B, C, D.** Front view, different magnifications. The sharpened tip apex with radius of curvature ∼25 nm is visible. Scale bars: B 1 µm, C 300 nm, D 50 nm.

mal tune method provided by the AFM controller. The spring constant lay consistently between 0.003 N/m and 0.007 N/m. AFM image data was processed in the Veeco Nanoscope 7.20 software. Cross-sectional profiles of rings were then extracted as graphs using the open source software Gwyddion (`http://gwyddion.net`). The profiles were then combined, averaged and analyzed by custom scripts in OriginPro 7.5 (OriginLab, USA).

3.5 Fluorescence microscopy

Fluorescence imaging was used to quickly and easily localize fluorescently labeled antibodies on the whole sample. The resolution of optical imaging is much lower than achievable by AFM and can be approximated by Abbe's equation:

$$d = \frac{\lambda}{2n \sin \alpha}\,, \tag{3.3}$$

where d is the minimal distance two objects can be distinguished as separate (also called the diffraction limit), λ is the imaging wavelength, n the refraction index of the lens, and α the opening angle of the objective, i.e. the angle from which light is able to be collected into the objective. $n \sin \alpha$ is also called the numerical aperture (NA) and indicated on

objectives. The diffraction limit for visible light imaging is $\sim 150 - 400\,\mathrm{nm}$, depending on the wavelengths and objectives used. Although the optical resolution limit does not allow discrimination of single antibodies or the exact determination of their position, the $1.3\,\mu\mathrm{m}$ distance between each nanoring is big enough to be able to tell whether the antibodies associate with a given nanoring or bind randomly to the glass surface between rings.

Fluorescence imaging works by exciting a fluorescent dye, so-called fluorophore, at one wavelength and measuring emitted light at a longer wavelength. See Fig. 3.8 for a more detailed explanation of the phenomenon. Every fluorophore has its specific excitation and emission wavelengths, so the optical measurement setup and the fluorophores have to be matched together. See Fig. 3.3 for a scheme of the optical setup. A fluorescence filtercube inside the microscope filters incoming light from a light source so that only the wavelengths needed to excite a specific fluorophore reach the sample. The same filtercube limits the emitted light from the sample to the emission wavelengths of the fluorophore before reaching the camera with which the image is recorded. A dichroic mirror with its reflectivity depending on the wavelength guides the excitation light to the sample and the emission light to the camera. By using different filtercubes with non-overlapping filter wavelengths it is possible to use several different fluorophores on the sample at the same time without the fluorescence from one affecting the other.

Fluorescence images were taken with a Leica DMI6000B inverted microscope (Leica Microsystems, Germany) which was modified to fit the Bioscope 2. Due to the integration of the AFM and optics on one stand, the sample did not have to be moved between AFM and fluorescence measurements, ensuring identical conditions for both imaging methods. A Leica $100\times$ oil-immersion objective with NA 1.46 was used with an additional tube magnification of $1.6\times$ to obtain the fluorescence images. A mercury lamp provided wide field fluorescence excitation of the sample. Optical filter cubes with bandpasses specific for the Alexa488 (excitation maximum at 496 nm, emission at 519 nm) and Cy3 (excita-

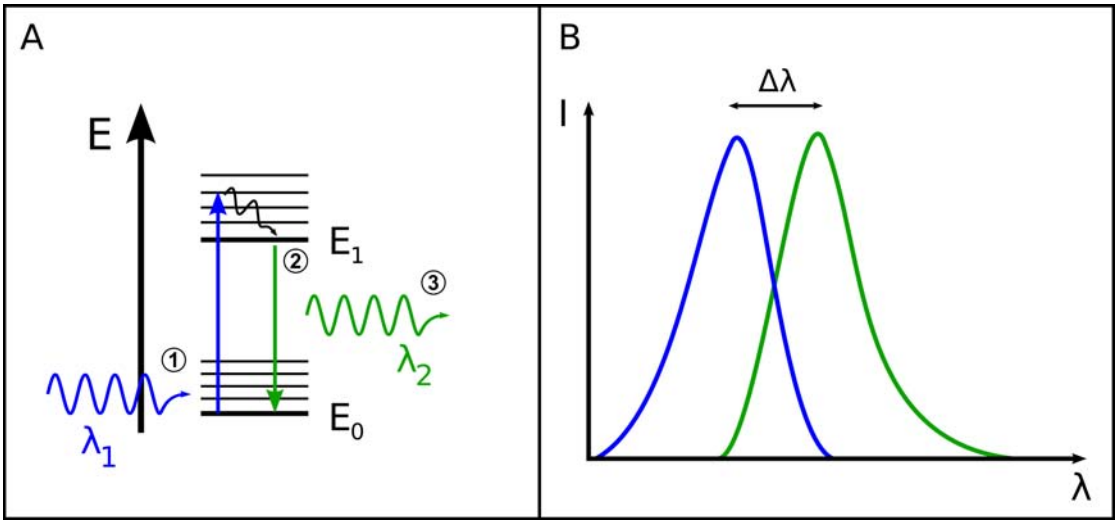

Figure 3.8: **A.** Working principle of fluorescence excitation and emission. **(1)** A fluorophore absorbs a photon of wavelength λ_1 and is excited from the ground state E_0 into a higher electronic energy state E_1. This absorption can only take place if the fluorophore has available energy states that can be reached with the energy of the incoming photon, thus limiting the possible excitation wavelengths. **(2)** Usually higher rotational and vibrational energy states (thin lines) are excited through photon absorption. These relax very fast (fs to ps time scale) in a non-radiative way to their ground state (e.g. by releasing heat into the surrounding medium) while the electronic excited state E_1 is longer living (ns time scale). This relaxation process is called internal conversion. **(3)** The molecule relaxes to its electronic ground state by emitting a photon. The emitted photon can never have higher energy than the absorbed one and, because of internal conversion, usually has a lower energy, i.e. higher wavelength λ_2. The difference between excitation and emission wavelength is called the Stokes shift. **B.** Relative excitation (blue) and emission (green) intensities as a function of wavelength. Any fluorophore absorbs and emits in a range of wavelengths with the highest excitation and emission at a given point. The difference $\Delta\lambda$ is again the Stokes shift.

tion 550 nm, emission 570 nm) fluorophores were used to excite only the desired molecules and to minimize background and gold autofluorescence (Chroma filterset numbers 41001 and 41007a, respectively; Chroma Technology, USA). Fluorescence images were taken with Leica DFC480 CCD camera in 16 bit monochrome mode, and processed and analyzed in ImageJ (`http://rsb.info.nih.gov/ij/`) (66) and GIMP (The Gnu Image Manipulation Program, `http://www.gimp.org/`).

Fluorescent images were obtained by incubating the nanorings sample at anti-PEG E11 concentrations of 10 pM – 10 nM for 30 min in darkness at room temperature, then rinsing the sample with 10 ml of PBS. AFM measurements were performed immediately after taking the fluorescence images.

4 Results

4.1 Mimicking the NPC topography

Cross-sectional profiles of bare rings were extracted from the height images obtained by contact mode AFM, overlaid on each other and then averaged (Fig. 4.1). This yielded 32.3 ± 2.4 nm, 371 ± 23 nm and 89 ± 18 nm for the height, outer diameter and inner diameter, respectively. We note that the AFM tip is able to penetrate completely into the central pore of the ring based on a tip radius of ~ 25 nm, although the inner and outer diameter of the rings is likely to suffer from tip convolution (Fig. 4.3A). The individual nanorings are spaced 1.3 µm apart to prevent any molecular interactions between rings. On each sample we therefore have 400 "experimental sites" that can be probed individually. The measurements confirm that we are able to reproducibly create nanostructures with similar dimensions as the NPC.

4.2 Polymer brush-barrier

Fig. 4.2 shows height measurements of the PEG-functionalized nanorings taken at the lowest possible force of 40 pN and with a very high force setpoint of 1400 pN. The difference in the two images is marked. At 40 pN, the nanoring appears to exhibit a "cloud-like" structure. A slight depression is visible only at the central pore. At 1400 pN the complete ring topography becomes visible again. Averaging over several cross-sections, the maximum height over the rings is 41.6 ± 1.9 nm and 31.5 ± 1.1 nm at 40 pN and 1400 pN,

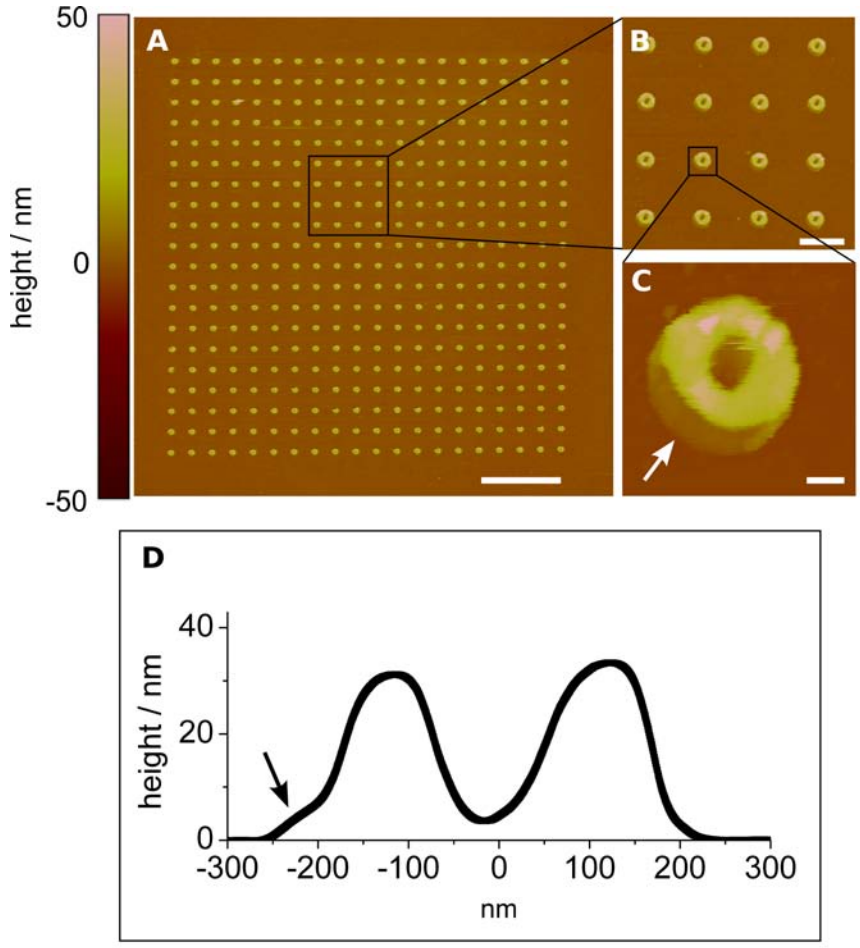

Figure 4.1: **A.** The AFM height image shows the 20×20 nanoring array. The distance of $1.3\,\mu$m between each ring ensures that PEG molecules do not interact between rings. **B, C.** Zoomed in scans from the preceding views. Scale bars: A, 5 µm. B, 1 µm. C, 100 nm. **D.** Cross-sectional profile shows the average dimensions of nanorings. Also visible is the 5 nm Cr adhesion layer which is not perfectly aligned with the top gold layer (arrow in C and D). Ring dimensions as measured by AFM: height 32.3 ± 2.4 nm, outer diameter 371 ± 23 nm, inner diameter 89 ± 18 nm.

respectively. The latter corresponds exactly to the height of a bare ring. By subtracting these values we get a brush height of $\sim 10\,\mathrm{nm}$. Interestingly, the outer diameter of the rings appears to be 39 nm wider on each side at 40 pN. This discrepancy between differences in height and width likely stems from the partial compression of the brush by the tip in z direction during imaging. Additionally, simulations of polymer brush interactions with an AFM tip have found that other geometric effects can also contribute to the under- and overestimation of polymer brush height and width by AFM (67, 68). A remarkable observation is that the tip is unable to penetrate the pore inspite of the lack of PEG chains at the base (SiO_2) of the central pore. See Fig. 4.3 for a to-scale illustration of the tip and brush interaction.

The presence of a brush over the rings and the hole is further confirmed by taking force-distance curves over different points of the sample (over glass, over the ring structure, over the pore) and looking at the repulsive forces acting on the cantilever. Fig. 4.4 shows representative force-distance curves. Curves taken over glass show no long-range repulsion but only the hard-wall repulsion at contact between glass and tip. In curves taken over a functionalized nanoring, a long-range repulsion can be measured starting 27 nm above the ring surface, which can be taken as a measure of the brush height. This measured height lies between the 10 nm and 39 nm measured by imaging in contact mode on top and on the sides of the rings, respectively. This also confirms the under- and overestimation of brush heights in contact mode as discussed above. Over the pore, the brush starts at 47 nm above the glass surface. Subtracting the ring height of 32 nm shows that the brush repulsion starts 15 nm above the ring surface, even when probing directly over the center of the pore.

4.3 Visualizing biochemical interactions via fluorescence

After confirming the presence of a steric repulsive brush over the nanorings, the effect of specific biochemical binding to the PEG chains was measured using fluorescence. The

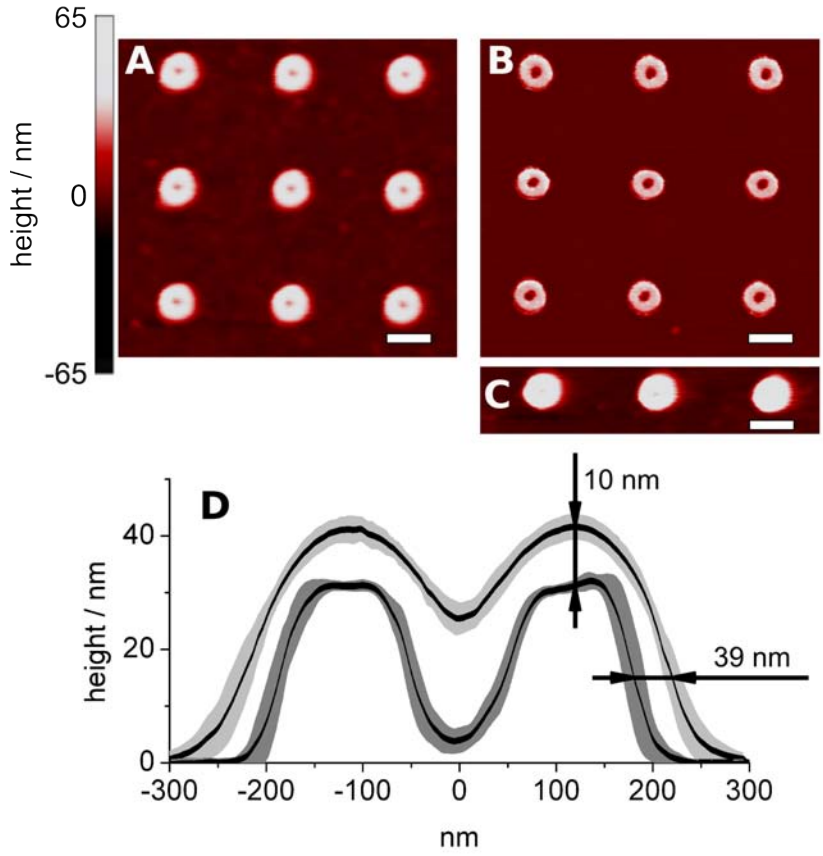

Figure 4.2: AFM height images of PEG-functionalized rings. **A.** When a low force (40 pN) is applied by the cantilever on the sample, the tip is not able to penetrate through the repulsive PEG brush-barrier. Note that the barrier is present at the center of the nanoring although no PEG molecules are anchored to the base of the pore (being SiO_2). **B.** At a higher applied force (1400 pN) the ring structure becomes clearly visible again. At this force, the tip is likely to have penetrated/displaced the PEG chains. **C.** When imaging the same rings with a low force again, the brush is restored. Scale bars, 500 nm. **D.** Cross-sectional profiles of rings with PEG at low (light gray) and high force (dark gray) show the extent of the brush. The black line denotes the mean after averaging, the gray shaded areas show the height standard deviation of the profiles.

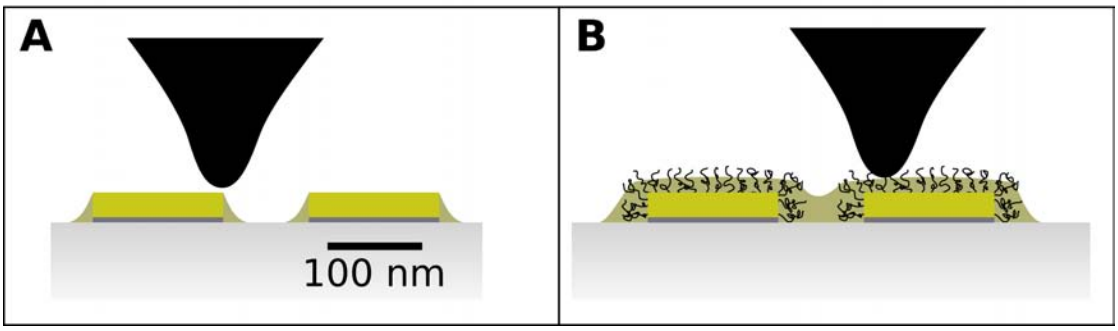

Figure 4.3: To-scale schematic illustrating the influence of tip shape and size on the nanoring measurements. **A.** The edges of the bare rings are likely to suffer from tip convolution effects as a result of the ~ 25 nm tip radius. Gray: Cr adhesion layer; bright yellow: Au nanoring; pale yellow: apparent shape as measured by AFM. **B.** With functionalized nanorings, the tip is sterically hindered from entering the central pore. The changes in the ring dimensions result from the presence of the PEG chains in spite of the same tip convolution effects.

fluorescence images after incubation with 10 nM E11(Fig. 4.5) show a clear site-specific localization of the fluorescence signal to the position of the Au nanorings. This confirms that the E11 antibody binds specifically to the PEG. At E11 concentrations lower than 10 nM no fluorescence was visible. This could be due to limitations of the optics or camera or possibly because of quenching effects of the gold rings (69). To verify that the fluorescence signal is specific to antibodies binding to PEG, several controls were carried out. These included: (i) measuring the fluorescence emission of the rings when no fluorophores were added to the sample (autofluorescence); and (ii) incubating an identical sample with unspecific antibodies labeled with Cy3 fluorophores (Fig. 4.5). Neither of the controls showed any significant fluorescence signal compared to the sample incubated with labeled E11.

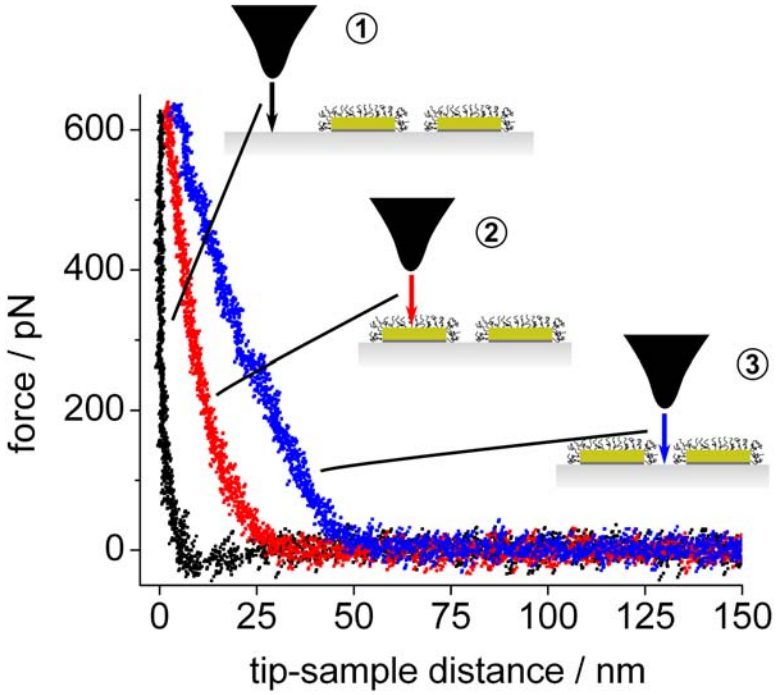

Figure 4.4: Three representative force-distance curves recorded over the glass, the ring and the pore, respectively. **(1)** The force curve on the glass shows hard-wall repulsion, i.e. no PEG. **(2)** Over a PEG-functionalized nanoring a repulsive force is felt by the cantilever 27 nm above the surface (zero is defined here as the gold surface of the ring). This is a direct measurement of the brush height within the limits of force sensitivity. **(3)** Over the pore a repulsive force is measured 47 nm above the glass, i.e. the repulsion from the PEG brush is felt by the cantilever 15 nm above the gold rings. This means that the brush is not as high as above the ring but still occludes the pore completely.

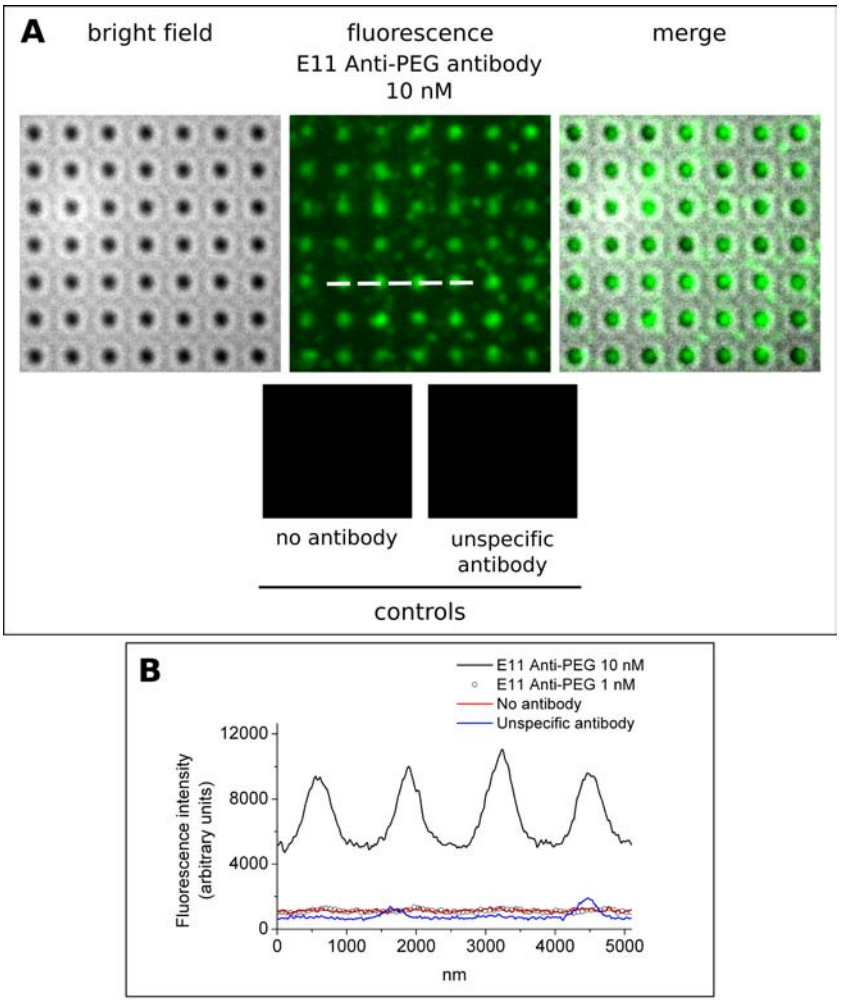

Figure 4.5: **A.** Fluorescent images taken after 30 min incubation with 10 nM anti-PEG E11 antibodies. The bright field image shows the position of the rings. The central pore cannot be resolved because of the diffraction limit. The fluorescence image shows the binding of anti-PEG to the PEG brush on the rings. Some unspecific adsorption to glass is also visible. The merged image confirms the localization of the labeled antibodies on the nanorings. Two negative controls show no fluorescence signal: gold rings with PEG but without any fluorescent antibodies, and fluorescently labeled unspecific antibodies. **B.** Fluorescence intensity profile representatively taken across four rings (indicated by dashed line). The labeled E11 has four clear peaks corresponding to the location of the rings at 10 nM. The elevated background comes from unspecific adsorption to glass and from fluorescence emission which is then scattered in the buffer. E11 at 1 nM and lower concentration shows no fluorescence.

4.4 Nanomechanical effects of binding to polymer brushes

Polymer brushes can reversibly collapse and extend when switching environmental conditions, e.g. exchange of a poor solvent for a good one (70). One of the key predictions of the entropic barrier model for nucleocytoplasmic transport is that FG nups collapse to their anchoring point upon binding one or several transport receptors (12).

In the current PEG/anti-PEG system, we obtain a clear difference between the low-force image of the brush only (Fig. 4.2) compared to the PEG with antibodies bound. Fig. 4.6 shows AFM data obtained directly after confirmation of antibody binding via fluorescence. We were not able to visualize individual antibodies, but the analysis of the cross-sectioned height profiles shows that the brush height decreases evenly on all sides of the ring to a height of $h_{\mathrm{ring}} = 36.4 \pm 1.7\,\mathrm{nm}$ (from 42 nm) and an outer diameter of 428 nm (from 466 nm). This is still $\sim$5 nm higher and $\sim$25 nm wider on each side than the bare rings or when imaged at a high force. This difference either indicates a partial collapse of the brush, or a complete collapse with the antibody piling up on top (see Fig. 4.7). Regardless, an interesting consequence of this collapse is the opening of the central pore, as shown in Fig. 4.6. This is in marked contrast to the closed pore conformation in the absence of E11. Clearly, antibody binding leads to a decrease in brush height at the center of the pore and hence to the opening of the pore. After incubation with anti-PEG, $w_{\mathrm{pore}} = 101\,\mathrm{nm}$. In comparison to a completely open pore ($w_{\mathrm{pore}} = 134\,\mathrm{nm}$ at 1400 pN), the tip is not able to penetrate the pore fully. This could be due to the accumulation of collapsed PEG chains and E11 within the pore itself.

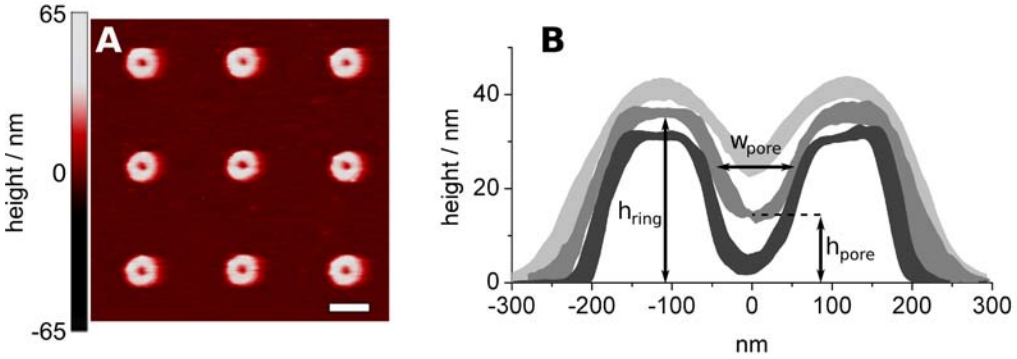

Figure 4.6: **A.** AFM height measurements after 30 min incubation with 10 nM anti-PEG E11. The measurements were taken at the lowest possible force (70 pN). Compared to Fig. 4.2, the PEG brush does not occlude the complete pore anymore but the ring structure is not as clearly visible as when imaging with high force either. **B.** Comparison of three different cross-sectional averages. From lightest to darkest: PEG-brush, no antibodies, low force (40 pN); PEG-brush, incubated with PEG antibodies, low force (70 pN); PEG-brush, no antibodies, high force (1400 pN). Compared to the PEG brush in the absence of E11, this shows clearly that the PEG collapses after binding to E11. The height difference between the collapsed state and the high force cross-section can be explained by the presence of antibodies on top of the rings and in the pore.

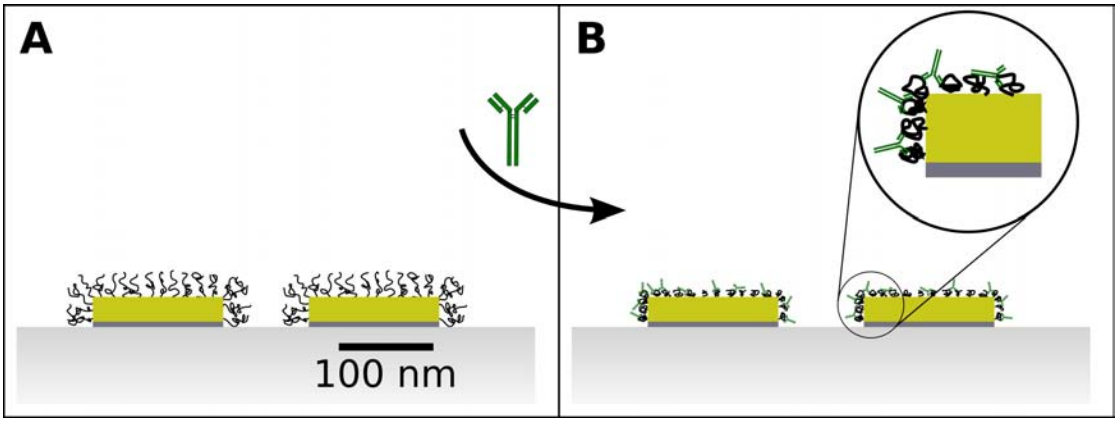

Figure 4.7: Possible mechanism for brush collapse on antibody binding. IgG antibodies have two binding sites, so one antibody can either bind two different PEG molecules or bind the same molecule at different positions on the backbone. Both scenarios would reduce the conformational freedom of the bound PEG chains and could lead to a collapse of the chains. The additional height of the collapsed state compared to bare rings (see Fig. 4.6) can be explained by a partial collapse of the brush (not drawn) or by the presence of bound E11 (B).

5 Discussion and Summary

First and foremost, we have shown that the PEG chains can give rise to a polymer brush that covers the nanorings and occludes the central pore. As shown in Figs. 4.2 and 4.4, the steric long-range repulsion of the PEG brush keeps the cantilever from entering the pore or tracing the ring structure at low forces. By increasing the applied force, the AFM tip seems to penetrate or splay the brush when moving over a ring. Switching back from high to low force shows again the brush which indicates that the PEG chains are only temporarily displaced by the tip but not removed from the rings. An important observation is that even though no PEG chains are attached to the base of the pore, the barrier is active over the whole pore, i.e. end-grafting PEG to the periphery of a pore is enough to establish a steric repulsive barrier over the pore itself. This barrier should be active for any macromolecule in the size of the tip ($\sim$25 nm hydrodynamic radius).

Controls with fluorescently labeled unspecific antibodies show no fluorescence on the rings after incubation and rinsing. This indicates that the PEG barrier prevents non-specific adsorption on the rings and clogging of the central pore even for smaller particles than the tip (the IgG hydrodynamic radius is $\sim$ 5 nm (71)). Further experiments are needed to address the exact role of the brush in preventing non-specific adsorption, e.g. AFM measurements after incubation with control antibodies as well as fluorescence measurements with different macromolecules with and without PEG on the rings.

By incubating our functionalized nanorings with anti-PEG, we have shown that it is possible to induce morphological changes in the PEG brush by specific biomolecular

interactions. Our AFM data (Fig. 4.6) suggests that anti-PEG binding to the PEG causes a significant collapse of the brush, with its height decreasing by 5 nm over the rings, i.e. 50 % of the total brush height, but keeping in mind that an exact brush height estimation solely by contact mode AFM is difficult. We observe the same 50 % reduction of the brush height also at the center of the pore, but the reduction in absolute terms (12 nm) is as expected much larger because no PEG is bound at the base itself.

We have established with AFM and fluorescence imaging that E11 anti-PEG is able to bind PEG in a brush conformation. IgG immunoglobulins have two antigen binding sites which seems to be already enough to induce a collapse (compared to importins with their 4 – 10 FG-binding sites). It is unlikely that a single antibody binding a PEG chain at one place could induce significant conformational changes in the chain, because except for some possible steric effects the conformational freedom of the chain should remain roughly the same, the antibody just moving along with the chain. But already one antibody binding two different chains or the antibody binding one chain at two distinct points of the backbone could limit the movement of the PEG which could then induce larger conformational changes in the chain, i.e. collapse.

Our observations show that the NPC transport mechanism can be replicated synthetically with non-NPC related molecules. Two main aspects of the "entropic barrier" model for nucleocytoplasmic transport – the steric entropic rejection of unspecific molecules and the translocation of targeted cargo via brush collapse (12, 72) – could be replicated in our PEG/anti-PEG system. Further, we could show that the steric repulsion over a pore is possible by polymers anchored to the periphery of the pore. Our results indicate that our experimental system is a valid basic model system for the NPC and can thus be used to explore the nature of the transport mechanism further, i.e. by varying different parameters such as pore geometry, functionalization and interacting molecules.

Perhaps even more importantly, our work can be seen as a proof of principle for the

feasibility of a nanopore or nanomembrane that bases its selectivity not on size exclusion or other general properties like charge, but on specific (bio-)molecular interactions between the pore and the molecule to be filtered or translocated. To be able to utilize a mechanism similar to the nucleocytoplasmic transport with artificial membranes would bring significant advantages compared to current technologies. For example, the economic savings in maintenance alone from non-clogging filters make pursuing this goal worthwhile. Additionally, an artificial membrane based on the NPC could introduce a completely new filtering paradigm, with specific targeted macromolecules being able to be filtered out from a solution. With this technique several new or enhanced applications would be possible, such as detection of hazardous substances (even things like specific viruses), accurate purification of specified proteins, or switchable flow control of filtration membranes. An artificial membrane based on the working principle of the NPC would combine the powerful filtering capabilities of the NPC with the relatively easy handling and advanced knowledge of polymers that exists today.

More generally, PEG- and anti-PEG interactions may be applied in drug delivery applications. There has been a growing interest into "smart" nanopores or hydrogels on polymer basis whereby changes in environmental parameters – such as pH or temperature – are used to selectively release drugs from a nanocontainer inside the body (73–75). Mostly the switching consists of opening and closing the pores without any selectivity or accurate control of release point. It has also been a challenge to find appropriate biocompatible polymers. Our results suggest that response of PEG brushes towards PEG-binding molecules could be harnessed for a more selective release of substances at the target site while maintaining biocompatibility and exploiting the "stealth" characteristics of PEG. Our PEG/anti-PEG system could also be used to provide a better understanding for the changes in drug retention times with PEGylated drugs and anti-PEG (45, 60), i.e. to elucidate the role of brush extension and collapse in these effects.

Last but not least, with our combination of nanostructures, fluorescence and AFM we were able to establish an assay that measures molecular binding and its effects directly at the nanometer scale. AFM measurements were performed directly after biochemical interactions had been induced and read out by fluorescence, without the need of sample transfer which often introduces undefined effects into the system. We were able to verify that our E11 antibodies bind specifically to PEG chains even when they are not in their "normal" dissolved conformation and then to look at the nanomechanical changes of the brush.

The use of nanofabrication allows for spatial control of the experiment at the relevant scale for molecular interactions. At these (mesoscopic) length scales, surface and interfacial effects play a dominant role and this cannot be neglected if one wants to gather an accurate image of interactions at this scale. By using nanofabrication, we can "look" at the behavior of biomolecules when they are present in similar numbers as in real biological systems. With this, we avoid issues of scaling when trying to translate macroscopic-sized or ensemble interaction assays as they are being used in many parts of molecular biology (e.g. gels/blots) to the mesoscopic scales of living cells. Further, the exploitation of nanofabrication allows the use of real three-dimensional structures without being limited to flat surfaces which is only an idealization of the real problem in many cases.

5.1 Future directions

Comparing our model system with the three main components of the nucleocytoplasmic transport system – FG-rich protein domains as the gate, transport receptors that bind to the FG-domains, and the cargo itself that binds to the transport receptor – we have established model counterparts for the gate and the transport receptors: the PEG brush and PEG antibodies, respectively. An obvious next step in constructing our model is to find an equivalent for cargo proteins. Secondary anti-mouse IgG antibodies provide fitting

binding specificity to our mouse IgG anti-PEG "transport receptor" without interacting with other parts of our sample. When labeled with a different fluorophore than the anti-PEG, future co-localization experiments with primary and secondary fluorescence emission (e.g. Alexa488 and Cy3 dyes) on our nanostructures could confirm that anti-PEG are able to bind the PEG-brush even when themselves bound by a secondary antibody acting as "cargo".

A final major enhancement in building a reduced, artificial NPC transport pathway is to replace the nanopore sitting on a glass surface with a functional membrane comprising pores in the same dimensions as described in this work (see Fig. 1.1 for a model). By functionalizing the pores with PEG and monitoring the membrane-separated reservoirs by fluorescence imaging, one could measure the flux of labeled primary and secondary antibodies across the PEG-gated membrane, thus addressing whether not only the polymers retract or collapse on binding but also if actual transport can occur through the pore. We have already obtained membranes with nanopores of 100 nm width and depth (Fig. 5.1A). The Si/SiN membranes are fabricated by etching the silicon backside up to the front SiN layer which is only 100 nm thick. Reactive ion etching is used to drill 100 nm wide holes into the membrane. Finally a layer of gold is evaporated on the front side to allow for functionalization of one side of the membrane.

We have also designed and commissioned a liquid cell that can hold the chip with the membrane between two channels with in- and outlets to introduce different solutions in defined concentrations (Fig. 5.1B). A clamping and sealing mechanism will hold the chip with the nanopores between the two halves of the liquid cell (Fig. 5.2). Optical grade polishing of the liquid cell made of quartz glass will allow for the measurement of fluorescence intensity on both sides of the chip. By functionalizing one side of the membrane with PEG chains we are hoping to establish a barrier over the pores against nonspecific molecules. After adding fluorescent primary and secondary antibodies, time-lapse monitoring of the relative fluorescence intensities in both halves should provide

us with transport kinetics. By varying PEG density, antibody concentration, or solvent composition and looking at changes in kinetics and flux through the membrane we want to get more insight into the transport mechanism. Experimental measurement could also be complemented by theoretical modeling or simulations of our system, enabling to quickly find out interesting parameters to vary or to look at in the experiments. It remains to be seen if PEG grafting on one side of the pores only is sufficient to block unspecific transport and to allow binding-specific facilitation of transport. With future nanofabrication processes we are looking to only evaporate gold around the pore entrances themselves, to functionalize both sides of the membrane or even the inside of the 100 nm long nanopores. The goal is the stepwise approach towards an even more accurate model of the NPC, and to optimize the filtering properties of the nanomembrane after it has been established that transport as described is indeed possible.

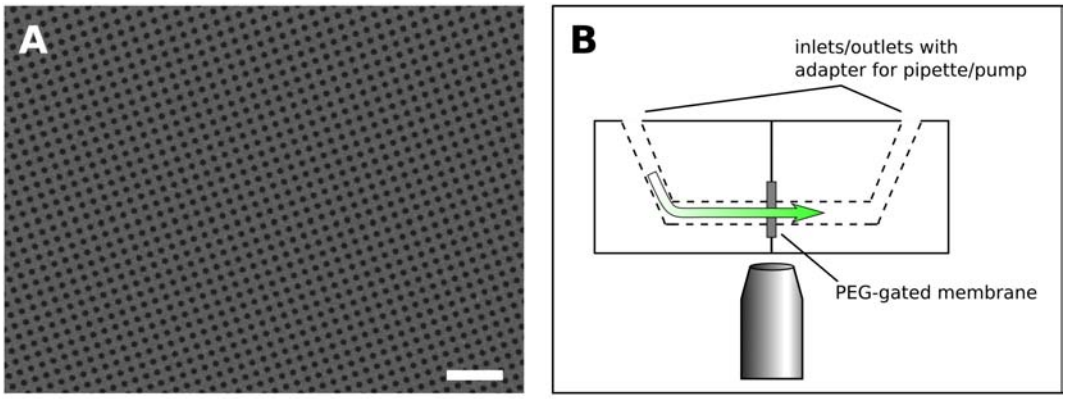

Figure 5.1: **A.** Scanning electron micrograph of the silicon nitride membrane with pores with a depth of 100 nm and a width of 100 nm. The whole surface on one side is covered with gold. Scale bar, 1 µm. **B.** Schematic of planned flux measurement system. The membrane is clamped between two halves of an optical grade quartz liquid cell. Inlets and outlets provide the means for introducing different solutes into the cell. Fluorescence optics from below the cell will be used to measure the relative fluorescence in both halves, providing information about bulk flux or kinetics.

Usual antibody binding strength is very high by virtue of their function inside their

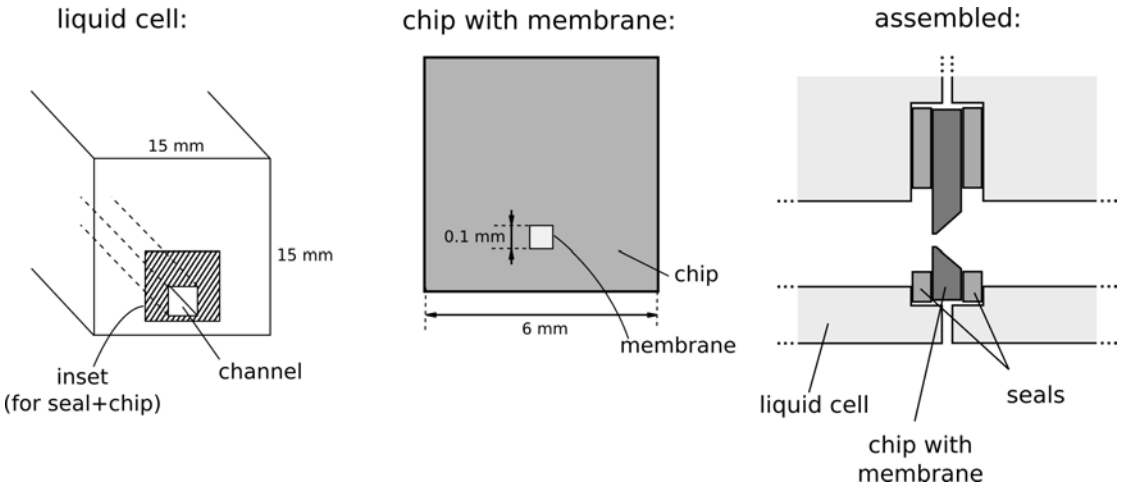

Figure 5.2: Detailed design of the chip with membrane and its assembly with the liquid cell (drawn not to scale). Thin (0.1 – 0.2 mm) teflon seals on both sides between liquid cell and chip prevent liquid leakage to the sides. A clamping mechanism applies pressure to the two halves of the liquid cell to keep the seal tight and prevent movement of the chip.

organisms and can be orders of magnitude stronger than interactions between the NPC transport constituents in the cell. This might pose a problem for observing flux through the pore. The antibodies could just stay bound to the pore for very long times, effectively either clogging the pore or opening it permanently. This can be alleviated by intentionally choosing antibodies that have been screened for weaker interaction with the antigen. The binding strength of antibodies can also be modified by changing solvent conditions, e.g. changing salt concentration or pH (76). Our proposed primary/secondary antibody system can also be modified or complemented by other molecules. Protein A and Protein G are known to bind the F_c part of IgG antibodies with different affinities (77, 78). By providing high enough concentrations of IgG binding molecules in solution, PEG-binding primary antibodies could potentially be sequestered away from the pore once they have passed the PEG gate to the other side. Experiments with PEG-binding IgM antibodies (61), which have 5 binding sites per antibody instead of two could provide information about the role of multivalency in pore translocation.

At the moment, our choice of PEG based on its unique properties limits the possible transport receptors to available anti-PEG proteins. An open question is the stability of the PEG/anti-PEG system under non-physiological conditions. While PEG is stable under various solvents (although not always forming a brush), the antibodies might degrade quickly under non-optimal conditions. A possible future direction is thus the design of other, more stable PEG-binding molecules.

5.2 Conclusions

In this work we have shown that PEG can form a brush-barrier over a nanopore even with no direct attachment points at the base of the pore. Specific binding to the PEG chains partially collapses the brush and opens up the pore, while unspecific molecules do not adsorb on or clog the pore. We have used the combination of nanofabrication, mechanical measurements by AFM, and fluorescence optics together to show a proof of principle how the highly efficient NPC selective gating mechanism between the nucleus and cytoplasm of a cell could be replicated with synthetic materials. The NPC gating is not based on size exclusion, as most of today's nanofilters, but on biochemical binding specificity. The ability to mimic the NPC transport mechanism with future synthetic nanofilters could ultimately lead to better and cheaper filtration systems. Besides acting as a model for future nanoporous membranes, these experiments indicate further that the NPC transport mechanism could indeed be using polymer brush-like structures to selectively gate the NPC pores and keep them from clogging.

5.3 Acknowledgments

I would like to thank first of all my supervisor Roderick Lim for his help and support throughout the whole project, and also of course for coming up with this project in the first place and offering it to me. I acknowledge our collaborator Deng Jie from IMRE in

Singapore who manufactured and provided all the nanostructures for this project, and continues to provide us with the nanopore membranes. Further I acknowledge Larisa Kapinos and Cora-Ann Schönenberger for help related to biochemical questions and issues, Larisa additionally for performing DLS measurements with PEG, Per Rigler for insights into fluorescence imaging and spectroscopy, Steve Roffler for providing the PEG antibodies for free, and Daniel Oeschger for support with various hardware from time to time. I also want to thank Unai Silvan for some troubleshooting and helpful hints. Finally, thanks also to all my lab mates for a pleasant and nice working atmosphere in the lab.

Bibliography

[1] Mark A Shannon, Paul W Bohn, Menachem Elimelech, John G Georgiadis, Benito J Mariñas, and Anne M Mayes. Science and technology for water purification in the coming decades. *Nature*, 452:301–10, March 2008.

[2] Joseph G. Jacangelo, R. Rhodes Trussell, and Montgomery Watson. Role of membrane technology in drinking water treatment in the united states. *Desalination*, 113:119–127, 1997.

[3] Tonni Agustiono Kurniawan, Wai-Hung Lo, and Gilbert Y S Chan. Physico-chemical treatments for removal of recalcitrant contaminants from landfill leachate. *Journal of hazardous materials*, 129:80–100, February 2006.

[4] Arunima Saxena, Bijay P Tripathi, Mahendra Kumar, and Vinod K Shahi. Membrane-based techniques for the separation and purification of proteins: an overview. *Advances in colloid and interface science*, 145:1–22, January 2009.

[5] Lauren F Greenlee, Desmond F Lawler, Benny D Freeman, Benoit Marrot, and Philippe Moulin. Reverse osmosis desalination: Water sources, technology, and today's challenges. *Water research*, 43:2317–48, May 2009.

[6] Ahmed Al-Amoudi and Robert W. Lovitt. Fouling strategies and the cleaning system of nf membranes and factors affecting cleaning efficiency. *Journal of Membrane Science*, 303:4–28, 2007.

[7] M Amiri and M Samiei. Enhancing permeate flux in a ro plant by controlling membrane fouling. *Desalination*, 207:361–369, 2007.

[8] F Reverberi and A Gorenflo. Three year operational experience of a spiral-wound swro system with a high fouling potential feed water. *Desalination*, 203:100–106, 2007.

[9] Murray Stewart. Molecular mechanism of the nuclear protein import cycle. *Nature reviews. Molecular cell biology*, 8:195–208, March 2007.

[10] Reiner Peters. Translocation through the nuclear pore: Kaps pave the way. *BioEssays : news and reviews in molecular, cellular and developmental biology*, 31:466–77, April 2009.

[11] Michael P Rout, John D Aitchison, Marcelo O Magnasco, and Brian T Chait. Virtual gating and nuclear transport: the hole picture. *Trends in cell biology*, 13:622–8, December 2003.

[12] Roderick Y H Lim, Birthe Fahrenkrog, Joachim Köser, Kyrill Schwarz-Herion, Jie Deng, and Ueli Aebi. Nanomechanical basis of selective gating by the nuclear pore complex. *Science*, 318:640–3, 2007.

[13] M Heuberger, T Drobek, and N D Spencer. Interaction forces and morphology of a protein-resistant poly(ethylene glycol) layer. *Biophysical journal*, 88:495–504, January 2005.

[14] D Leckband, S R Sheth, and A Halperin. Grafted poly(ethylene oxide) brushes as nonfouling surface coatings. *Journal of biomaterials science. Polymer edition*, 10:1125–47, January 1999.

[15] Daniel P Denning, Samir S Patel, Vladimir Uversky, Anthony L Fink, and Michael F Rexach. Disorder in the nuclear pore complex: the fg repeat regions of nucleoporins are natively unfolded. *Proceedings of the National Academy of Sciences of the United States of America*, 100:2450–5, March 2003.

[16] Daniel Stoffler, Bernhard Feja, Birthe Fahrenkrog, Jochen Walz, Dieter Typke, and Ueli Aebi. Cryo-electron tomography provides novel insights into nuclear pore architecture: Implications for nucleocytoplasmic transport. *Journal of Molecular Biology*, 328:119–130, April 2003.

[17] Frank Alber, Svetlana Dokudovskaya, Liesbeth M Veenhoff, Wenzhu Zhang, Julia Kipper, Damien Devos, Adisetyantari Suprapto, Orit Karni-Schmidt, Rosemary Williams, Brian T Chait, Andrej Sali, and Michael P Rout. The molecular architecture of the nuclear pore complex. *Nature*, 450:695–701, November 2007.

[18] Samir S Patel, Brian J Belmont, Joshua M Sante, and Michael F Rexach. Natively unfolded nucleoporins gate protein diffusion across the nuclear pore complex. *Cell*, 129:83–96, April 2007.

[19] Laura J Terry, Eric B Shows, and Susan R Wente. Crossing the nuclear envelope: hierarchical regulation of nucleocytoplasmic transport. *Science*, 318:1412–6, November 2007.

[20] J N Bright, T B Woolf, and J H Hoh. Predicting properties of intrinsically unstructured proteins. *Progress in biophysics and molecular biology*, 76:131–73, July 2001.

[21] Roderick Y H Lim, Joachim Köser, Ning-Ping Huang, Kyrill Schwarz-Herion, and Ueli Aebi. Nanomechanical interactions of phenylalanine-glycine nucleoporins studied by single molecule force-volume spectroscopy. *Journal of structural biology*, 159:277–89, August 2007.

[22] R Bayliss, T Littlewood, and Murray Stewart. Structural basis for the interaction between fxfg nucleoporin repeats and importin-beta in nuclear trafficking. *Cell*, 102:99–108, July 2000.

[23] Richard Bayliss, Sara W Leung, Rosanna P Baker, B Booth Quimby, Anita H Corbett, and Murray Stewart. Structural basis for the interaction between ntf2 and nucleoporin fxfg repeats. *The EMBO journal*, 21:2843–53, 2002.

[24] Timothy A Isgro and Klaus Schulten. Binding dynamics of isolated nucleoporin repeat regions to importin-beta. *Structure (London, England : 1993)*, 13:1869–79, December 2005.

[25] Roderick Y H Lim and Ueli Aebi. In silico access to the nuclear pore complex. *Structure (London, England : 1993)*, 13:1741–3, December 2005.

[26] Steffen Frey and Dirk Görlich. A saturated fg-repeat hydrogel can reproduce the permeability properties of nuclear pore complexes. *Cell*, 130:512–23, 2007.

[27] S T Milner. Polymer brushes. *Science*, 251:905–914, February 1991.

[28] P. G. De Gennes. Conformations of polymers attached to an interface. *Macromolecules*, 13:1069–1075, September 1980.

[29] P. G. De Gennes. Polymers at an interface; a simplified view. *Advances in colloid and interface science*, 27:189–209, 1987.

[30] B. Zhao and W. J. Brittain. Polymer brushes: surface-immobilized macromolecules. *Progress in Polymer Science*, 25:33, 2000.

[31] P.G. De Gennes. Scaling theory of polymer adsorption. *Journal de Physique*, 37:1445–1452, 1976.

[32] S. Alexander. Adsorption of chain molecules with a polar head a scaling description. *Journal de Physique*, 38:983–987, 1977.

[33] N A Alcantar, E S Aydil, and J N Israelachvili. Polyethylene glycol-coated biocompatible surfaces. *Journal of biomedical materials research*, 51:343–51, September 2000.

[34] J Israelachvili. The different faces of poly(ethylene glycol). *Proceedings of the National Academy of Sciences of the United States of America*, 94:8378–9, August 1997.

[35] Hongbin Li, Matthias Rief, Filipp Oesterhelt, and Hermann E. Gaub. Single molecule force spectroscopy by afm indicates helical structure of poly(ethyleneglycol) in water. *Advanced Materials*, 10:316–319, 1999.

[36] Ferry Kienberger, Vassili Ph. Pastushenko, Gerald Kada, Hermann J. Gruber, Christian Riener, Hansgeorg Schindler, and Peter Hinterdorfer. Static and dynamical properties of single poly(ethylene glycol) molecules investigated by force spectroscopy. *Single Molecules*, 1:123–128, June 2000.

[37] M Rief, M Gautel, F Oesterhelt, J M Fernandez, and H E Gaub. Reversible unfolding of individual titin immunoglobulin domains by afm. *Science*, 276:1109–12, May 1997.

[38] A F Oberhauser, P E Marszalek, H P Erickson, and J M Fernandez. The molecular elasticity of the extracellular matrix protein tenascin. *Nature*, 393:181–5, May 1998.

[39] K J Ryan and S R Wente. The nuclear pore complex: a protein machine bridging the nucleus and cytoplasm. *Current opinion in cell biology*, 12:361–71, June 2000.

[40] H Ju, Bryan D. McCloskey, Alyson C. Sagle, Y Wu, Victor A. Kusuma, and Benny D Freeman. Crosslinked poly(ethylene oxide) fouling resistant coating materials for oil/water separation. *Journal of Membrane Science*, 307:260–267, January 2008.

[41] Hao Ju, Bryan D. McCloskey, Alyson C. Sagle, Victor A. Kusuma, and Benny D Freeman. Preparation and characterization of crosslinked poly(ethylene glycol) diacrylate hydrogels as fouling-resistant membrane coating materials. *Journal of Membrane Science*, 330:180–188, 2009.

[42] D L Elbert and J A Hubbell. Reduction of fibrous adhesion formation by a copolymer possessing an affinity for anionic surfaces. *Journal of biomedical materials research*, 42:55–65, 1998.

[43] K D Park, Y S Kim, D K Han, Y H Kim, E H Lee, H Suh, and K S Choi. Bacterial adhesion on peg modified polyurethane surfaces. *Biomaterials*, 19:851–9, 1998.

[44] Buddy D Ratner and Stephanie J Bryant. Biomaterials: where we have been and where we are going. *Annual review of biomedical engineering*, 6:41–75, January 2004.

[45] Richard B Greenwald, Yun H Choe, Jeffrey McGuire, and Charles D Conover. Effective drug delivery by pegylated drug conjugates. *Advanced drug delivery reviews*, 55:217–50, February 2003.

[46] A Abuchowski, J R McCoy, N C Palczuk, T Van Es, and F F Davis. Effect of covalent attachment of polyethylene glycol on immunogenicity and circulating life of bovine liver catalase. *The Journal of biological chemistry*, 252:3582–6, June 1977.

[47] G Fontana, M Licciardi, S Mansueto, D Schillaci, and G Giammona. Amoxicillin-loaded polyethylcyanoacrylate nanoparticles: influence of peg coating on the particle size, drug release rate and phagocytic uptake. *Biomaterials*, 22:2857–65, November 2001.

[48] R Gref, A Domb, P. Quellec, T. Blunk, R. H. Müller, J. M. Verbavatz, and R. Langer. The controlled intravenous delivery of drugs using peg-coated sterically stabilized nanospheres. *Advanced Drug Delivery Reviews*, 16:215–233, September 1995.

[49] M C Woodle, M S Newman, and J A Cohen. Sterically stabilized liposomes: physical and biological properties. *Journal of drug targeting*, 2:397–403, 1994.

[50] Andrew P Chapman. Pegylated antibodies and antibody fragments for improved therapy: a review. *Advanced drug delivery reviews*, 54:531–45, June 2002.

[51] S Lee, R B Greenwald, J McGuire, K Yang, and C Shi. Drug delivery systems employing 1,6-elimination: releasable poly(ethylene glycol) conjugates of proteins. *Bioconjugate chemistry*, 12:163–9, 2001.

[52] Valentina Rapozzi, Susanna Cogoi, Paola Spessotto, Angela Risso, Gian Maria Bonora, Franco Quadrifoglio, and Luigi Emilio Xodo. Antigene effect in k562 cells of a peg-conjugated triplex-forming oligonucleotide targeted to the bcr/abl oncogene. *Biochemistry*, 41:502–10, January 2002.

[53] Samuel Zalipsky. Functionalized poly(ethylene glycols) for preparation of biologically relevant conjugates. *Bioconjugate Chemistry*, 6:150–165, March 1995.

[54] David K. Male, Jonathan Brostoff, Ivan Maurice Roitt, and David Roth. *Immunology*. Elsevier Health Sciences, 7 edition, 2006.

[55] David Goodsell. Igg volume rendering. RCSB Protein Data Bank. URL: `http://www.pdb.org/pdb/static.do?p=education_discussion/molecule_of_the_month/pdb21_1.html`. Accessed: 2009-07-09. (Archived at `http://www.webcitation.org/5i8I6FlhE`), 2001.

[56] G Köhler and C Milstein. Continuous cultures of fused cells secreting antibody of predefined specificity. *Nature*, 256:495–7, August 1975.

[57] M Feldmann and R N Maini. Anti-tnf alpha therapy of rheumatoid arthritis: what have we learned? *Annual review of immunology*, 19:163–96, January 2001.

[58] J Mendelsohn and J Baselga. The egf receptor family as targets for cancer therapy. *Oncogene*, 19:6550–65, December 2000.

[59] P Carter. Improving the efficacy of antibody-based cancer therapies. *Nature reviews. Cancer*, 1:118–29, November 2001.

[60] Tian-Lu Cheng, Chiu-Min Cheng, Bing-Mae Chen, Der-An Tsao, Kuo-Hsiang Chuang, Sheng-Wen Hsiao, Yi-Hung Lin, and Steve R Roffler. Monoclonal antibody-based quantitation of poly(ethylene glycol)-derivatized proteins, liposomes, and nanoparticles. *Bioconjugate chemistry*, 16:1225–31, 2005.

[61] N M Tsai, Tian-Lu Cheng, and Steve R Roffler. Sensitive measurement of polyethylene glycol-modified proteins. *BioTechniques*, 30:396–402, February 2001.

[62] Tian-Lu Cheng, Bing-Mae Chen, J W Chern, M F Wu, and Steve R Roffler. Efficient clearance of poly(ethylene glycol)-modified immunoenzyme with anti-peg monoclonal antibody for prodrug cancer therapy. *Bioconjugate chemistry*, 11:258–66, 2000.

[63] Tian-Lu Cheng, P Y Wu, M F Wu, J W Chern, and Steve R Roffler. Accelerated clearance of polyethylene glycol-modified proteins by anti-polyethylene glycol igm. *Bioconjugate chemistry*, 10:520–8, 1999.

[64] David a Wunderlich, Margit Macdougall, Diane V Mierz, Joshuaine G Toth, Thomas M Buckholz, Kevin J Lumb, and Haren Vasavada. Generation and characterization of a monoclonal igg antibody to polyethylene glycol. *Hybridoma (2005)*, 26:168–72, June 2007.

[65] Wolfgang Schärtl. *Light Scattering from Polymer Solutions and Nanoparticle Dispersions*. Springer, 2007.

[66] M D Abramoff, P J Magalhaes, and S J Ram. Image processing with imagej. *Biophotonics International*, 11:36–43, 2004.

[67] Michael Patra and Per Linse. Reorganization of nanopatterned polymer brushes by the afm measurement process. *Macromolecules*, 39:4540–4546, June 2006.

[68] Michael Patra and Per Linse. Simulation of grafted polymers on nanopatterned surfaces. *Nano letters*, 6:133–7, January 2006.

[69] E. Dulkeith, a. Morteani, T. Niedereichholz, T. A. Klar, J. Feldmann, S. Levi, F. Van Veggel, D. Reinhoudt, M Möller, and D. Gittins. Fluorescence quenching of dye molecules near gold nanoparticles: Radiative and nonradiative effects. *Physical Review Letters*, 89:12–15, November 2002.

[70] Shashishekar P. Adiga and Donald W. Brenner. Virtual molecular design of an environment-responsive nanoporous system. *Nano Letters*, 2:567–572, 2002.

[71] W Hartmann, Nirmala Saptharishi, Xiao Yi Yang, Gautam Mitra, and Gopalan Soman. Characterization and analysis of thermal denaturation of antibodies by size exclusion high-performance liquid chromatography with quadruple detection. *Analytical Biochemistry*, 325:227–239, 2004.

[72] Roderick Y H Lim, Ning-Ping Huang, Joachim Köser, Jie Deng, K H Aaron Lau, Kyrill Schwarz-Herion, Birthe Fahrenkrog, and Ueli Aebi. Flexible phenylalanine-glycine nucleoporins as entropic barriers to nucleocytoplasmic transport. *Proceedings of the National Academy of Sciences of the United States of America*, 103:9512–7, June 2006.

[73] Liang-Yin Chu, Sang-Hoon Park, Takeo Yamaguchi, and Shin-ichi Nakao. Preparation of thermo-responsive core-shell microcapsules with a porous membrane and poly(n-isopropylacrylamide) gates. *Journal of Membrane Science*, 192:27–39, 2001.

[74] Xia Cao, Siyi Lai, and L. James Lee. Design of a self-regulated drug delivery device. *Biomedical Microdevices*, 3:109 – 118, 2001.

[75] Yong Song Park, Yoshihiro Ito, and Yukio Imanishi. Photocontrolled gating by polymer brushes grafted on porous glass filter. *Macromolecules*, 31:2606–2610, April 1998.

[76] NC Hughes-Jones, B Gardner, and R Telford. The effect of ph and ionic strength on the reaction between anti-d and erythrocytes. *Immunology*, 75:507–12, March 1964.

[77] J Sjödahl. Structural studies on the four repetitive fc-binding regions in protein a from staphylococcus aureus. *European journal of biochemistry / FEBS*, 78:471–90, September 1977.

[78] U Sjöbring, L Björck, and W Kastern. Streptococcal protein g. gene structure and protein binding properties. *The Journal of biological chemistry*, 266:399–405, May 1991.